The Astrophysical Journal Supplement Series, 179:423–450, 2008 December

THE FORMATION AND EVOLUTION OF PLANETARY SYSTEMS: DESCRIPTION OF THE *SPITZER* LEGACY SCIENCE DATABASE

John M. Carpenter,[1] Jeroen Bouwman,[2] Murray D. Silverstone,[3] Jinyoung Serena Kim,[4] John Stauffer,[5] Martin Cohen,[6] Dean C. Hines,[7] Michael R. Meyer,[4] and Nathan Crockett[8]

Received 2008 March 31; accepted 2008 July 26

ABSTRACT

We present the science database produced by the Formation and Evolution of Planetary Systems (FEPS) *Spitzer* Legacy program. Data reduction and validation procedures for the IRAC, MIPS, and IRS instruments are described in detail. We also derive stellar properties for the FEPS sample from available broadband photometry and spectral types, and present an algorithm to normalize Kurucz synthetic spectra to optical and near-infrared photometry. The final FEPS data products include IRAC and MIPS photometry for each star in the FEPS sample and calibrated IRS spectra.

Subject headings: circumstellar matter — infrared: stars — planetary systems: formation

Online material: tar file

1. INTRODUCTION

The Formation and Evolution of Planetary Systems (FEPS) *Spitzer* Legacy program (Meyer et al. 2006) was designed to characterize the evolution of circumstellar gas and dust around solar-type stars between ages of 3 Myr and 3 Gyr. To achieve these goals, FEPS obtained spectrophotometric observations with the *Spitzer Space Telescope* (Werner et al. 2004) for a sample of 328 stars (see Meyer et al. 2006 for a description of the sample). The observing strategy was to measure the spectral energy distribution (SED) between wavelengths of 3.6 and 70 μm with IRAC (Infrared Array Camera; Fazio et al. 2004) and MIPS (Multiband Imaging Photometer for *Spitzer*; Rieke et al. 2004) photometry, and between 8 and 35 μm with low-resolution IRS (Infrared Spectrograph; Houck et al. 2004) spectra. In addition, the FEPS program obtained MIPS 160 μm photometry for 80 stars to search for colder dust, and high-resolution IRS spectra for 33 sources to probe for circumstellar gas.

The FEPS team has produced several studies on the incidence of dusty debris disks around solar type stars, including the discovery of a debris system in the initial *Spitzer* observations (Meyer et al. 2004), a census of warm debris (Stauffer et al. 2005; Silverstone et al. 2006; Hines et al. 2006; Meyer et al. 2008), the identification of Kuiper Belt analogs (Kim et al. 2005; Hillenbrand et al. 2008), and an investigation of debris disks around stars with known planets (Moro-Martín et al. 2007). The FEPS team has also analyzed the processing of dust in optically thick, primordial disks (Bouwman et al. 2008), and has produced a series of papers on the evolution of gas in solar-type stars (Hollenbach et al. 2005; Pascucci et al. 2006, 2007).

This paper describes the data reduction procedures for IRAC (3.6, 4.5, and 8 μm) and MIPS (24 and 70 μm) images and IRS low-resolution spectra obtained by the FEPS program. Data reduction methods for the MIPS 160 μm images and IRS high-resolution spectra are discussed in Kim et al. (in preparation) and Pascucci et al. (2006), respectively. The adopted reduction procedures for the IRAC, MIPS 24 μm, MIPS 70 μm, and IRS observations are presented in §§ 2–5. We also investigate the effects of source confusion on the 24 and 70 μm photometry (§ 6) and the relative calibration accuracy between *Spitzer* instruments (§ 7). The series of FEPS papers frequently utilized synthetic spectra derived from Kurucz model atmospheres to infer the presence of infrared excesses diagnostic of circumstellar dust. In the Appendices, we describe the data and algorithm used to obtain normalized synthetic spectra for individual stars. The primary data products from the FEPS program are a tabulation of IRAC and MIPS photometry presented in Table 1, and extracted, calibrated spectra which are available electronically.

2. IRAC

IRAC produces images in four channels at wavelengths of 3.6, 4.5, 5.8, and 8.0 μm with bandwidths of 0.75, 1.01, 1.42, and 2.93 μm, respectively (Fazio et al. 2004). The FEPS team obtained IRAC observations for 311 of the 328 stars in the sample. The remaining 17 objects were observed by other *Spitzer* programs, including 16 Hyades stars in a Guaranteed Time Observations (GTO) program led by G. Fazio, and one source (ScoPMS 214) in the Upper Sco OB Association by the c2d Legacy Program (Evans et al. 2003).

FEPS IRAC observations were conducted in subarray mode with a four-point dither pattern and the medium dither scale. The locations of the four dither positions on the array are the same for each source to within the pointing accuracy of the spacecraft ($1\,\sigma < 1''$ radial; Werner et al. 2004). In subarray mode, each IRAC band is observed separately where a 32×32 pixel section ($39'' \times 39''$) in a corner of the 256×256 pixel full-array ($5.2' \times 5.2'$) is read out at frame times of 0.02, 0.10, or 0.40 s. At each dither position, 64 images are taken at the same frame time for a total of 256 images per band, with the same frame time for each band and a given source. The total on-source integration time per band is then 5.12, 25.6, and 102.4 s for frame times of 0.02, 0.10, and 0.40 s, respectively. The frame time was selected on a source-by-source basis to achieve a high signal-to-noise ratio (S/N) on the stellar photosphere without saturating the detector. Five FEPS

[1] Department of Astronomy, California Institute of Technology, Mail Code 105-24, 1200 East California Boulevard, Pasadena, CA 91125.
[2] Max-Planck-Institut für Astronomie, D-69117 Heidelberg, Germany.
[3] Eureka Scientific Inc., 113 Castlefern Drive, Cary NC 25713.
[4] Steward Observatory, The University of Arizona, 933 North Cherry Avenue, Tucson, AZ 85721.
[5] *Spitzer* Science Center, California Institute of Technology, Mail Code 314-6, 1200 East California Boulevard, Pasadena, CA 91125.
[6] Radio Astronomy Laboratory, University of California, Berkeley, CA 94720.
[7] Space Science Institute, 4750 Walnut Street, Suite 205, Boulder, CO 80301.
[8] Department of Astronomy, University of Michigan, Ann Arbor, MI 48109.

TABLE 1
IRAC AND MIPS PHOTOMETRY

	IRAC						MIPS									
	3.6 μm		4.5 μm		8 μm		24 μm		70 μm		IRAC Frame Time	MIPS 24μm DCE Time	AOR Key		Flags[a]	
Source	S_ν (mJy)	$\sigma_{\rm int}$ (mJy)	S_ν (mJy)	$\sigma_{\rm int}$ (mJy)	S_ν (mJy)	$\sigma_{\rm int}$ (mJy)	S_ν (mJy)	$\sigma_{\rm int}$ (mJy)	S_ν (mJy)	$\sigma_{\rm int}$ (mJy)	(s)	(s)	IRAC	MIPS	IRAC	MIPS
1E 0307.4+1424	91.21	0.66	57.60	0.70	20.51	0.14	2.60	0.03	−10.8	5.4	0.40	9.96	5296896	5297408		
1E 0324.1−2012	86.59	0.62	55.47	0.68	19.53	0.13	2.50	0.02	−1.7	3.7	0.40	9.96	5297664	5298176		
1RXS J025216.9+361658	321.18	2.31	202.24	2.47	77.25	0.51	8.81	0.08	−0.6	4.3	0.10	9.96	5256960	5257472		2
1RXS J025751.8+115759	121.01	0.87	76.26	0.93	27.93	0.18	3.27	0.04	1.3	5.4	0.10	9.96	5261568	5262080		
1RXS J030759.1+302032	313.33	2.26	196.62	2.40	71.77	0.47	8.13	0.08	2.0	5.0	0.10	2.62	5313536	5314048		
1RXS J031644.0+192259	55.94	0.40	35.50	0.43	12.87	0.09	1.57	0.03	−9.4	5.9	0.40	9.96	5302272	5302784		
1RXS J031907.4+393418	47.01	0.34	29.19	0.36	10.88	0.07	1.31	0.02	−3.0	4.3	0.40	9.96	5257728	5258240		
1RXS J034423.3+281224	389.93	2.81	246.84	3.01	88.38	0.58	10.01	0.09	−0.4	5.5	0.10	2.62	5258496	5259008		
1RXS J035028.0+163121	107.74	0.78	68.39	0.83	24.39	0.16	2.95	0.03	−10.1	6.6	0.10	9.96	5263104	5263616		
1RXS J043243.2−152003	106.89	0.77	66.74	0.81	23.97	0.16	2.92	0.03	−2.4	3.5	0.10	9.96	5244416	5244928		
1RXS J051111.1+281353	223.49	1.61	139.47	1.70	53.61	0.35	7.77	0.07	1.4	11.0	0.10	2.62	5246720	5247232		
1RXS J053650.0+133756	179.78	1.29	112.07	1.37	41.56	0.27	4.93	0.04	−0.2	11.0	0.10	9.96	5247488	5248000		
2RE J0255+474	396.39	2.85	248.21	3.03	90.62	0.60	10.30	0.09	−1.3	4.6	0.10	2.62	5349632	5350144	1	
AO Men	568.24	4.09	359.74	4.81	130.52	0.86	16.16	0.15	4.9	3.4	0.02	2.62	5222144	5222656		
AP 93	56.05	0.40	34.91	0.43	12.96	0.09	1.62	0.02	5.3	10.2	0.40	9.96	5282304	5282816		
B102	88.83	0.68	56.44	0.77	20.52	0.14	2.54	0.11	−15.0	22.1	0.40	9.96	5275392	5275904		
BPM 87617	234.87	1.69	148.05	1.81	54.85	0.36	6.59	0.06	−3.0	4.3	0.10	2.62	5348864	5349376		
HD 105	1022.72	7.36	645.37	7.87	230.66	1.52	28.29	0.25	141.2	10.4	0.02	2.62	5295360	5295872		
HD 377	1029.07	7.41	648.56	7.91	234.70	1.67	36.58	0.33	162.0	12.6	0.02	2.62	5268480	5268992		
HD 691	967.52	6.97	597.48	7.29	218.32	1.44	25.01	0.23	8.3	7.2	0.02	2.62	5345024	5345536		
HD 984	1050.29	7.56	662.15	8.08	236.77	1.56	26.88	0.24	−9.4	8.4	0.02	2.62	5271552	5272064		2
HD 6434	952.27	6.86	603.33	7.36	215.10	1.42	23.95	0.22	8.0	7.4	0.02	2.62	5439232	5439744		
HD 6963	1211.31	8.72	752.85	9.19	271.46	1.79	32.53	0.29	44.0	8.0	0.02	2.62	5395712	5396224		
HD 7661	1428.00	10.28	887.28	10.82	322.51	2.13	36.03	0.32	4.4	7.9	0.02	2.62	5370624	5371136		
HD 8907	1918.20	13.81	1223.73	14.93	427.28	2.82	51.28	0.46	247.4	9.3	0.02	2.62	5361920	5362432		2
HD 8941	2006.73	14.45	1266.43	15.45	448.80	2.96	49.89	0.45	4.5	9.3	0.02	2.62	5413888	5414400		
HD 9472	1088.63	7.84	678.21	8.27	242.00	1.60	27.28	0.25	1.1	9.5	0.02	2.62	5391872	5392384		
HD 11850	952.41	6.86	595.66	7.27	211.74	1.78	24.05	0.22	−4.0	9.6	0.02	2.62	5375232	5375744		
HD 12039	747.34	5.38	470.88	5.75	170.38	1.13	25.65	0.23	3.5	8.1	0.02	2.62	5310464	5310976		
HD 13382	1391.67	10.02	881.73	10.76	313.35	2.07	36.27	0.33	3.2	9.5	0.02	2.62	5372928	5373440		
HD 13507	1715.75	12.35	1071.21	13.07	389.82	2.57	42.99	0.39	4.4	7.4	0.02	2.62	5390336	5390848		
HD 13531	1552.04	11.18	964.04	11.76	349.37	2.31	39.14	0.35	1.8	8.0	0.02	2.62	5372160	5372672		
HD 13974	14705.79	105.88	9279.19	113.21	3299.77	21.78	374.1	3.4	46.0	9.0	0.02	2.62	5410816	5411328		
HD 15526	182.75	1.32	113.77	1.39	40.84	0.27	4.89	0.04	−4.5	3.9	0.10	9.96	5263872	5264384		
HD 17925	7280.60	52.42	4520.57	55.15	1644.56	10.85	193.6	1.7	57.0	11.6	0.02	2.62	5306112	4036352		4
HD 18940	1815.57	13.07	1130.20	13.79	405.23	2.67	45.58	0.41	−4.7	9.9	0.02	2.62	5388032	5388544		
HD 19019	1664.30	11.98	1050.85	12.82	371.56	2.45	42.21	0.38	3.9	10.3	0.02	2.62	5407232	5407744		
HD 19668	605.66	5.12	382.24	4.66	134.35	1.01	18.74	0.17	−2.0	9.2	0.02	2.62	5340416	5340928		
HD 21411	1008.04	7.26	627.22	7.65	225.56	1.49	25.14	0.23	3.8	7.6	0.02	2.62	5389568	5390080		
HD 22179	311.69	2.24	196.20	2.39	71.03	0.47	11.10	0.10	35.9	10.3	0.10	2.62	5262336	5262848		
HD 25300	649.30	4.67	398.75	4.87	152.33	1.41	18.61	0.17	0.7	4.8	0.02	2.62	5350400	5350912		
HD 25457	6259.72	45.07	3956.34	48.27	1412.34	9.32	205.8	1.9	307.2	9.2	0.02	2.62	5308160	5308672		
HD 26182	227.33	1.64	144.51	1.76	52.11	0.34	5.94	0.07	1.6	8.8	0.10	2.62	5358848	5359360	1	

TABLE 1—*Continued*

Source	IRAC 3.6 μm S_ν (mJy)	IRAC 3.6 μm σ_{int} (mJy)	IRAC 4.5 μm S_ν (mJy)	IRAC 4.5 μm σ_{int} (mJy)	IRAC 8 μm S_ν (mJy)	IRAC 8 μm σ_{int} (mJy)	MIPS 24 μm S_ν (mJy)	MIPS 24 μm σ_{int} (mJy)	MIPS 70 μm S_ν (mJy)	MIPS 70 μm σ_{int} (mJy)	IRAC Frame Time (s)	MIPS 24μm DCE Time (s)	AOR Key IRAC	AOR Key MIPS	Flags[a] IRAC	Flags[a] MIPS
HD 26990	1286.97	9.27	804.17	9.81	289.30	1.91	32.75	0.29	9.4	9.0	0.02	2.62	5391104	5391616		
HD 27466	883.45	6.36	557.40	6.80	198.51	1.31	21.90	0.20	1.7	7.6	0.02	2.62	5411584	5412096		
HD 28495	1463.51	10.54	911.59	11.12	331.19	2.19	38.13	0.34	−7.0	10.3	0.02	2.62	5366016	5366528		
HD 29231	1332.22	9.59	821.42	10.02	297.62	1.96	33.14	0.30	3.8	7.2	0.02	2.62	5405696	5406208		
HD 31143	900.01	6.48	556.10	6.78	203.33	1.34	22.69	0.20	2.9	7.8	0.02	2.62	5401088	5401600		
HD 31281	271.15	1.95	171.58	2.09	62.45	0.41	7.43	0.09	9.6	13.4	0.10	2.62	5254912	5255424		
HD 31392	1431.93	10.31	891.69	10.88	321.84	2.12	36.88	0.33	81.6	8.4	0.02	2.62	5398016	5398528		
HD 31950	130.03	0.94	83.02	1.01	29.00	0.24	3.69	0.04	−2.7	8.9	0.10	9.96	5303808	5304320	1	
HD 32850	1487.55	10.71	929.44	11.34	336.42	2.22	38.37	0.35	2.2	11.9	0.02	2.62	5402624	5403136		
HD 35850	3030.34	21.82	1917.88	23.40	690.67	4.56	83.52	0.75	40.3	7.5	0.02	2.62	5446912	5447424		
HD 37006	740.10	5.33	465.45	5.68	164.16	1.08	18.64	0.17	−2.1	6.2	0.02	2.62	5388800	5389312		
HD 37216	1122.32	8.08	694.71	8.47	250.81	1.66	28.03	0.25	6.7	9.3	0.02	2.62	5386496	5387008		
HD 37484	893.68	6.43	568.11	7.50	202.23	1.59	54.59	0.49	114.4	7.8	0.02	2.62	5306624	5307136		
HD 37572	1362.34	9.81	848.38	10.35	310.18	2.05	35.26	0.32	5.7	7.6	0.02	2.62	6601472	6599680		
HD 37962	883.69	6.36	553.46	6.75	198.17	1.45	22.62	0.20	16.5	7.4	0.02	2.62	5412352	5412864		
HD 38207	286.99	2.07	181.35	2.21	64.62	0.43	16.46	0.15	184.6	4.7	0.10	2.62	5363200	5363712		
HD 38529	5893.09	42.43	3634.04	44.34	1339.97	8.84	149.6	1.3	75.3	11.2	0.02	2.62	5436928	5437440		
HD 38949	775.76	5.58	488.07	5.95	172.26	1.16	20.02	0.18	7.2	8.0	0.02	2.62	5339648	5340160		
HD 40647	872.61	6.28	543.42	6.63	195.98	1.29	22.11	0.20	7.0	6.7	0.02	2.62	5384192	5384704		
HD 41700	2693.24	19.39	1696.38	20.70	613.28	4.05	71.78	0.65	22.2	7.6	0.02	2.62	5365248	5365760		
HD 43989	719.52	5.18	454.19	5.54	163.22	1.21	21.14	0.19	7.1	9.8	0.02	2.62	6600704	6598912		
HD 44594	2593.89	18.68	1606.66	19.60	587.33	3.88	63.92	0.58	5.3	6.7	0.02	2.62	5444608	5445120		
HD 45270	2675.06	19.26	1698.63	20.72	599.85	3.96	70.18	0.63	8.5	6.0	0.02	2.62	6601216	6599424		2
HD 47875	364.71	2.95	230.96	3.70	81.40	2.08	9.70	0.09	0.0	3.7	0.02	2.62	5293824	5294336	1	
HD 60737	910.07	6.55	569.23	6.95	202.08	1.51	24.10	0.22	17.7	11.1	0.02	2.62	5267712	5268224		
HD 61005	753.53	5.42	472.32	5.76	169.19	1.12	41.49	0.37	628.7	11.1	0.02	2.62	5266944	5267456		
HD 61994	2103.13	15.14	1291.84	17.11	471.04	3.11	51.98	0.47	6.9	6.9	0.02	2.62	5394176	5394688		
HD 64324	929.20	6.69	585.16	7.14	207.22	1.37	23.76	0.21	6.3	9.9	0.02	2.62	5400320	5400832		
HD 66751	2683.46	19.32	1682.98	20.53	600.21	3.96	66.35	0.60	6.0	7.2	0.02	2.62	5408768	5409280		
HD 69076	791.83	5.70	492.67	6.01	177.87	2.21	20.14	0.18	0.4	8.4	0.02	2.62	5421568	5422080		2
HD 70516	995.64	7.17	623.34	7.61	227.16	1.50	25.38	0.23	8.4	6.9	0.02	2.62	5292288	5292800		
HD 70573	381.64	2.75	239.73	2.92	86.39	0.57	10.41	0.09	14.8	5.7	0.10	2.62	5308928	5309440		
HD 71974	1889.06	13.60	1168.70	14.26	423.82	2.80	47.65	0.43	16.4	7.9	0.02	2.62	5393408	5393920		
HD 72687	590.63	4.25	369.65	4.51	133.01	1.44	18.80	0.17	3.2	8.7	0.02	2.62	6600448	6598656		2
HD 72905	6226.53	44.83	3915.21	47.77	1411.52	9.32	163.5	1.5	44.5	5.4	0.02	2.62	5362688	4042240		4
HD 73668	1401.43	10.09	881.16	10.75	313.64	2.07	35.39	0.32	10.5	10.4	0.02	2.62	5435392	5435904		
HD 75302	1315.76	9.47	819.18	9.99	293.72	1.94	32.70	0.29	1.4	8.6	0.02	2.62	5404160	5404672		
HD 75393	1244.85	8.96	787.10	9.60	281.09	1.85	31.70	0.29	−6.2	9.0	0.02	2.62	5341184	5341696		
HD 76218	1329.90	9.57	833.15	10.16	300.52	1.98	33.66	0.30	−5.1	10.0	0.02	2.62	5373696	5374208		
HD 77407	1910.85	13.76	1211.53	14.78	444.45	2.93	49.20	0.44	11.1	9.3	0.02	2.62	5311232	5311744		
HD 80606	339.01	2.44	210.02	2.56	75.52	0.50	8.65	0.08	3.4	5.2	0.10	2.62	5443840	5444352		
HD 85301	1050.80	7.57	652.06	7.96	234.22	2.30	36.80	0.33	38.5	7.0	0.02	2.62	5399552	5400064		
HD 86356	186.44	1.34	117.14	1.43	42.97	0.28	5.12	0.05	−2.6	4.3	0.10	9.96	5260032	5260544		
HD 88201	1022.26	7.36	644.98	7.87	229.89	1.52	25.62	0.23	−1.2	7.3	0.02	2.62	5347328	5347840		

TABLE 1—*Continued*

Source	IRAC 3.6 μm S_ν (mJy)	IRAC 3.6 μm σ_{int} (mJy)	IRAC 4.5 μm S_ν (mJy)	IRAC 4.5 μm σ_{int} (mJy)	IRAC 8 μm S_ν (mJy)	IRAC 8 μm σ_{int} (mJy)	MIPS 24 μm S_ν (mJy)	MIPS 24 μm σ_{int} (mJy)	MIPS 70 μm S_ν (mJy)	MIPS 70 μm σ_{int} (mJy)	IRAC Frame Time (s)	MIPS 24μm DCE Time (s)	AOR Key IRAC	AOR Key MIPS	Flags[a] IRAC	Flags[a] MIPS
HD 88742	2966.24	21.36	1865.15	22.75	663.21	4.38	73.26	0.66	8.4	8.9	0.02	2.62	5422336	5422848		
HD 90712	1043.36	7.51	666.66	8.13	235.39	1.55	26.13	0.24	−2.7	8.0	0.02	2.62	5337344	5337856		
HD 90905	1788.78	12.88	1126.18	13.74	401.52	2.65	49.73	0.45	22.3	11.4	0.02	2.62	5335808	5336320		
HD 91782	573.48	4.13	361.12	4.41	127.76	1.36	14.78	0.13	−1.9	7.5	0.02	2.62	5331200	5331712		
HD 91962	2018.84	14.54	1264.75	15.43	457.91	3.02	50.77	0.46	−0.4	7.8	0.02	2.62	5341952	5342464	1	
HD 92788	1447.46	10.42	891.20	10.87	322.72	2.13	36.08	0.32	11.2	9.1	0.02	2.62	5440000	5440512		
HD 92855	1280.32	9.22	810.92	9.89	288.82	1.91	32.43	0.29	9.8	6.8	0.02	2.62	5331968	5332480		
HD 95188	627.15	4.51	391.95	4.78	140.03	0.92	15.95	0.14	6.1	9.5	0.02	2.62	5344256	5344768		
HD 98553	1067.94	7.69	669.07	8.16	238.75	1.58	26.35	0.24	3.9	8.0	0.02	2.62	5408000	5408512		
HD 100167	1361.36	9.80	855.45	10.44	307.60	2.03	34.35	0.31	−2.9	8.7	0.02	2.62	5420032	5420544		
HD 101472	1036.87	7.46	665.02	8.11	233.44	1.77	26.19	0.24	−0.6	8.8	0.02	2.62	5342720	5343232		
HD 101959	1612.53	11.61	1013.24	12.36	361.27	2.38	40.18	0.36	9.8	8.4	0.02	2.62	5418496	5419008		
HD 102071	1103.79	7.95	679.71	8.29	246.67	1.63	27.71	0.25	9.5	7.4	0.02	2.62	5423104	5423616		
HD 103432	676.31	4.87	425.79	5.20	150.78	1.13	16.82	0.15	8.4	9.8	0.02	2.62	5428480	5428992		
HD 104467	535.57	3.86	336.17	4.10	121.77	0.88	14.16	0.13	−1.9	5.0	0.02	2.62	5208320	5208832		2
HD 104576	616.98	4.44	383.90	4.68	142.62	1.60	16.22	0.15	6.9	8.0	0.02	2.62	5332736	5333248		
HD 104860	724.76	5.22	455.33	5.55	162.49	1.13	19.89	0.18	183.1	7.4	0.02	2.62	5270016	5270528		
HD 105631	1613.93	11.62	989.25	12.07	360.21	2.38	40.27	0.36	1.0	7.4	0.02	2.62	5415424	5415936		
HD 106156	1012.92	7.29	623.21	7.60	227.72	1.50	25.47	0.23	15.1	9.3	0.02	2.62	5423872	5424384		
HD 106252	1200.09	8.64	746.45	9.11	270.92	1.79	30.58	0.28	16.5	9.4	0.02	2.62	5442304	5442816		
HD 106772	992.21	7.14	630.40	7.69	232.27	1.85	26.40	0.24	−4.6	6.8	0.02	2.62	5301504	5302016		
HD 107146	1711.29	12.32	1074.76	13.11	384.40	2.54	59.76	0.54	669.1	9.6	0.02	2.62	5312000	5312512		
HD 107441	254.97	1.84	161.86	1.98	58.42	0.39	7.24	0.07	1.6	7.2	0.10	2.62	5234432	5234944		
HD 108799	3417.14	24.60	2165.72	26.42	767.08	5.06	85.26	0.77	5.0	10.2	0.02	2.62	5338112	5338624	1	
HD 108944	1136.76	8.19	727.64	8.88	256.94	1.70	28.88	0.26	1.7	8.4	0.02	2.62	5334272	5334784	1	
HD 111170	373.25	2.69	234.54	3.14	86.24	0.57	10.27	0.09	−4.9	9.2	0.10	2.62	5213696	5214208		
HD 112196	1734.86	12.49	1098.91	13.41	395.59	2.61	43.62	0.39	3.2	9.1	0.02	2.62	5278464	5278976	1	
HD 115043	2122.18	15.28	1336.87	16.31	476.04	3.14	53.18	0.48	−0.5	7.8	0.02	2.62	6600960	6599168		
HD 116099	111.96	0.81	70.52	0.86	25.38	0.17	3.53	0.03	3.4	3.3	0.10	9.96	5229056	5229568		
HD 117524	223.38	1.61	139.71	1.70	51.23	0.34	6.12	0.06	−10.1	9.9	0.10	9.96	5231360	5231872		
HD 119269	267.91	1.93	168.94	2.06	61.61	0.41	7.40	0.07	21.6	10.5	0.10	2.62	5239040	5239552		
HD 120812	200.55	1.44	127.58	1.56	46.06	0.30	5.57	0.05	−8.9	7.9	0.10	9.96	5227520	5228032		
HD 121320	928.87	6.69	581.52	7.09	209.87	1.39	23.04	0.21	2.1	9.7	0.02	2.62	5424640	5425152		
HD 121504	1001.83	7.21	630.62	7.69	225.25	1.49	25.01	0.23	27.2	18.7	0.02	2.62	5437696	5438208		
HD 122652	1260.59	9.08	795.28	9.70	283.09	1.87	35.22	0.32	83.1	9.1	0.02	2.62	5427712	5428224		
HD 126670	216.52	1.56	137.21	1.67	49.79	0.33	6.17	0.07	−0.8	5.7	0.10	2.62	5212928	5213440		
HD 128242	224.73	1.62	143.13	1.75	52.02	0.34	6.32	0.06	−6.3	5.8	0.10	9.96	5226752	5227264		
HD 129333	1252.51	9.02	790.35	9.64	285.15	1.88	32.83	0.30	6.3	6.3	0.02	2.62	5265409	5265920		
HD 132173	913.26	6.58	577.37	7.04	205.21	1.35	24.11	0.22	−0.8	9.9	0.02	2.62	5333504	5334016		
HD 133295	1343.76	9.68	852.62	10.40	301.06	1.99	34.10	0.31	12.2	12.4	0.02	2.62	5366784	5367296		
HD 133938	128.42	0.93	81.78	1.00	29.60	0.20	3.48	0.03	−5.0	11.5	0.10	9.96	5280768	5281280		
HD 134319	548.74	3.95	339.31	4.14	121.37	0.80	15.41	0.14	−3.4	8.1	0.02	2.62	5307392	5307904		
HD 135363	1045.48	7.53	660.17	8.05	241.28	2.27	28.18	0.25	0.1	7.1	0.02	2.62	5293056	5293568		
HD 136923	2175.65	15.66	1356.06	16.54	489.09	3.23	54.16	0.49	11.3	7.6	0.02	2.62	5429248	5429760		

TABLE 1—*Continued*

Source	IRAC 3.6 μm S_ν (mJy)	IRAC 3.6 μm σ_{int} (mJy)	IRAC 4.5 μm S_ν (mJy)	IRAC 4.5 μm σ_{int} (mJy)	IRAC 8 μm S_ν (mJy)	IRAC 8 μm σ_{int} (mJy)	MIPS 24 μm S_ν (mJy)	MIPS 24 μm σ_{int} (mJy)	MIPS 70 μm S_ν (mJy)	MIPS 70 μm σ_{int} (mJy)	IRAC Frame Time (s)	MIPS 24μm DCE Time (s)	AOR Key IRAC	AOR Key MIPS	Flags[a] IRAC	Flags[a] MIPS
HD 138004	1208.71	8.70	749.81	9.15	269.34	1.78	29.76	0.27	1.6	7.3	0.02	2.62	5433088	5433600		
HD 139498	287.36	2.07	181.71	2.22	66.48	0.44	7.89	0.10	−7.4	15.7	0.10	2.62	5228288	5228800		
HD 139813	1843.07	13.27	1151.04	14.04	419.79	2.77	46.37	0.42	15.6	7.7	0.02	2.62	5336576	5337088		
HD 140374	224.05	1.61	139.56	1.70	50.59	0.33	5.79	0.05	−12.3	11.7	0.10	9.96	5224448	5224960		
HD 141521	245.93	1.77	153.00	1.87	56.64	0.37	6.70	0.07	−10.6	12.5	0.10	2.62	5225216	5225728		
HD 141937	1392.65	10.03	872.31	10.64	310.76	2.05	34.94	0.31	−2.8	11.6	0.02	2.62	5441536	5442048		
HD 141943	849.12	6.11	541.02	6.60	193.09	1.47	27.34	0.25	37.6	15.0	0.02	2.62	5252608	5253120		
HD 142229	690.86	4.97	438.40	5.35	152.19	1.13	17.70	0.16	2.8	8.5	0.02	2.62	5384960	5385472		
HD 142361	459.81	3.31	292.68	3.57	107.66	0.80	12.74	0.11	12.2	19.4	0.02	2.62	5241344	5241856		
HD 143006	1069.37	7.70	929.86	11.34	792.11	5.23	3258	29	3795.1	33.3	0.02	2.62	5197312	5197824		
HD 143358	173.57	1.25	111.01	1.35	40.14	0.28	5.22	0.05	2.1	14.8	0.10	9.96	5236736	5237248		
HD 145229	1128.81	8.13	717.36	8.75	254.00	1.68	31.02	0.28	64.4	7.3	0.02	2.62	5387264	5387776		
HD 146516	203.17	1.46	129.34	1.58	46.83	0.31	5.79	0.05	4.1	11.4	0.10	9.96	5218304	5218816		
HD 150554	820.15	5.91	523.93	6.39	181.49	1.58	20.50	0.18	−6.6	6.9	0.02	2.62	5443072	5443584		
HD 150706	1715.11	12.35	1077.03	13.14	388.12	2.56	44.93	0.40	41.3	8.0	0.02	2.62	5385728	5386240		
HD 151798	746.39	5.37	467.61	5.71	166.72	1.10	18.67	0.17	−5.0	16.9	0.02	2.62	5276160	5276672		
HD 152555	819.35	5.90	515.58	6.29	185.47	1.22	20.59	0.19	−0.5	9.6	0.02	2.62	5330432	5330944	1	
HD 153458	742.93	5.35	465.17	5.67	165.26	1.15	18.90	0.17	−5.4	11.6	0.02	2.62	5416192	5416704		
HD 154417	3993.62	28.75	2506.84	30.58	897.07	5.92	100.9	0.9	5.2	8.5	0.02	2.62	5398784	5399296		
HD 157664	616.87	4.44	391.44	4.78	136.12	0.90	15.36	0.14	3.1	8.2	0.02	2.62	5445376	5445888		
HD 159222	2730.18	19.66	1715.21	20.93	613.30	4.05	67.39	0.61	5.6	7.2	0.02	2.62	5436160	5436672		
HD 161897	1217.95	8.77	754.95	9.21	273.67	1.81	30.18	0.27	−1.8	11.6	0.02	2.62	5430016	5430528		
HD 167389	1210.09	8.71	762.22	9.30	269.59	1.78	29.97	0.27	−4.4	9.2	0.02	2.62	5433856	5434368		
HD 170778	1076.58	7.75	681.74	8.32	241.21	1.59	27.23	0.25	3.9	6.3	0.02	2.62	5369856	5370368		
HD 172649	929.58	6.69	595.15	7.26	208.44	2.24	23.82	0.21	−1.2	7.7	0.02	2.62	5335040	5335552		
HD 174656	362.01	2.61	227.08	2.77	83.19	0.55	10.25	0.09	1.6	4.5	0.10	2.62	5195776	5196288		
HD 179949	2942.99	21.19	1849.03	22.56	658.41	4.34	73.94	0.67	−4.8	10.6	0.02	2.62	5440768	5441280		
HD 183216	1430.42	10.30	896.03	10.93	320.78	2.12	39.41	0.35	22.8	10.2	0.02	2.62	5401856	5402368		
HD 187897	1495.45	10.77	934.10	11.40	338.68	2.23	39.79	0.36	61.6	8.2	0.02	2.62	5419264	5419776		
HD 190228	2068.09	14.89	1282.73	15.65	469.44	3.10	52.77	0.47	11.7	25.5	0.02	2.62	5438464	5438976		
HD 191089	1071.72	7.72	678.37	8.28	242.17	1.60	185.6	1.7	544.3	12.5	0.02	2.62	5363968	5364224		
HD 193017	1179.47	8.49	743.73	9.07	264.71	1.75	29.90	0.27	6.6	9.3	0.02	2.62	5410048	5410560		
HD 195034	1689.95	12.17	1060.98	12.94	379.42	2.50	41.94	0.38	1.6	8.4	0.02	2.62	5426176	5426688		
HD 199019	745.17	5.37	473.60	5.78	165.29	1.09	18.93	0.17	9.0	7.8	0.02	2.62	5343488	5344000		
HD 199143	1401.22	10.09	899.64	10.98	320.68	2.42	37.60	0.34	9.2	11.1	0.02	2.62	5254144	5254656	1	
HD 199598	1843.53	13.27	1165.87	14.22	412.16	2.72	46.64	0.42	6.9	7.8	0.02	2.62	5413120	5413632		
HD 200746	814.31	5.86	519.15	6.33	183.35	1.30	20.80	0.19	11.4	8.1	0.02	2.62	5371392	5371904		
HD 201219	816.37	5.88	508.54	6.20	181.28	1.20	21.97	0.20	42.4	7.2	0.02	2.62	5396480	5396992		2
HD 201989	1440.45	10.37	902.15	11.01	323.35	2.13	36.16	0.33	−0.2	9.5	0.02	2.62	5394944	5395456	1	
HD 202108	1440.33	10.37	902.09	11.01	321.78	2.12	35.98	0.32	−0.3	9.6	0.02	2.62	5416960	5417472		
HD 202917	519.16	3.74	320.83	3.91	117.29	1.44	19.20	0.17	37.1	5.9	0.02	2.62	5251328	4558848		4
HD 203030	613.14	4.42	382.11	4.66	137.07	0.91	15.56	0.14	6.5	7.4	0.02	2.62	5338880	5339392		
HD 204277	1847.54	13.30	1172.19	14.30	415.82	2.74	48.88	0.44	29.6	10.6	0.02	2.62	5374464	5374976		
HD 205905	2172.60	15.64	1366.13	16.67	491.11	3.24	54.34	0.49	17.1	8.9	0.02	2.62	5404928	5405440		

TABLE 1—*Continued*

Source	IRAC 3.6 μm S_ν (mJy)	IRAC 3.6 μm σ_{int} (mJy)	IRAC 4.5 μm S_ν (mJy)	IRAC 4.5 μm σ_{int} (mJy)	IRAC 8 μm S_ν (mJy)	IRAC 8 μm σ_{int} (mJy)	MIPS 24 μm S_ν (mJy)	MIPS 24 μm σ_{int} (mJy)	MIPS 70 μm S_ν (mJy)	MIPS 70 μm σ_{int} (mJy)	IRAC Frame Time (s)	MIPS 24μm DCE Time (s)	AOR Key IRAC	AOR Key MIPS	Flags[a] IRAC	Flags[a] MIPS
HD 206374	1389.08	10.00	871.06	10.63	312.08	2.06	35.22	0.32	18.1	6.7	0.02	2.62	5414656	5415168		
HD 209253	2008.37	14.46	1285.28	15.68	454.49	3.00	55.94	0.50	75.0	9.2	0.02	2.62	5364480	5364992		
HD 209393	856.52	6.17	531.63	6.49	192.30	1.84	21.74	0.20	−2.4	9.0	0.02	2.62	5368320	5368832		
HD 209779	1295.17	9.32	812.17	9.91	292.11	2.16	32.90	0.30	9.8	11.6	0.02	2.62	5369088	5369600		
HD 212291	907.89	6.54	570.73	6.96	205.97	1.36	22.72	0.20	8.0	7.6	0.02	2.62	5420800	5421312		
HD 216275	1379.27	9.93	867.30	10.58	309.52	2.04	34.54	0.31	7.3	10.5	0.02	2.62	5434624	5435136		2
HD 216803	8665.98	62.40	5318.78	64.89	1969.21	13.00	224.3	2.0	27.5	5.3	0.02	2.62	5255680	4058624		4
HD 217343	1252.13	9.02	782.38	9.54	282.44	1.86	32.64	0.29	−0.8	9.2	0.02	2.62	5269248	5269760		
HD 219498	313.21	2.25	196.15	2.39	70.45	0.47	10.53	0.09	22.8	3.7	0.10	2.62	5357312	5357824		
HD 224873	625.86	4.51	388.50	4.74	140.78	0.93	15.50	0.14	−6.7	8.5	0.02	2.62	5346560	5347072	1	
HD 245567	277.75	2.00	175.57	2.14	64.72	0.43	7.32	0.08	−27.0	17.5	0.10	2.62	5248256	5248768		
HD 279788	118.00	0.85	74.32	0.91	26.84	0.18	3.52	0.03	2.6	11.4	0.10	9.96	5245952	5246464		
HD 281691	133.87	1.10	83.68	1.02	30.45	0.20	4.12	0.04	−1.8	6.1	0.10	9.96	5259264	5259776		
HD 282346	306.09	2.20	190.62	2.33	70.26	0.46	8.19	0.08	−20.3	10.3	0.10	2.62	5303040	5303552		
HD 284135	237.70	1.71	149.74	1.83	53.60	0.35	6.36	0.08	7.8	5.8	0.10	2.62	5206784	5207296		
HD 284266	110.21	0.79	69.84	0.85	24.99	0.17	3.14	0.03	−2.9	12.6	0.10	9.96	5220608	5221120		
HD 285281	280.25	2.02	176.07	2.15	64.82	0.43	7.80	0.08	−1.9	4.6	0.10	2.62	5216000	5216512		
HD 285372	93.54	0.67	58.77	0.72	21.50	0.17	2.55	0.03	−4.5	9.4	0.10	9.96	5209856	5210368		
HD 285751	91.46	0.66	56.25	0.70	20.74	0.17	2.64	0.03	−2.2	11.0	0.10	9.96	5207552	5208064		
HD 285840	102.52	0.74	64.06	0.78	23.50	0.15	2.81	0.03	−3.1	7.4	0.40	9.96	5359616	5360128		
HD 286179	124.11	0.89	77.97	0.95	28.01	0.18	3.28	0.04	−4.6	9.3	0.10	9.96	5221376	5221888		
HD 286264	267.39	1.93	167.19	2.04	62.31	0.41	7.56	0.09	−6.8	8.0	0.10	2.62	5250560	5251072		
HE 350	56.95	0.41	36.36	0.44	13.10	0.09	1.63	0.02	6.0	9.8	0.40	9.96	5283072	5283584		
HE 373	51.15	0.37	32.44	0.40	11.87	0.08	1.42	0.02	−3.0	4.6	0.40	9.96	5283840	5284352		
HE 389	46.64	0.34	29.26	0.36	10.55	0.07	1.22	0.02	−0.1	10.4	0.40	9.96	5284608	5285120		
HE 622	44.63	0.32	28.14	0.34	10.31	0.07	1.21	0.02	1.9	10.7	0.40	9.96	5285376	5285888		
HE 696	39.98	0.29	25.79	0.32	9.12	0.06	1.07	0.02	−20.2	11.0	0.40	9.96	5286144	5286656		
HE 699	51.39	0.37	32.70	0.40	11.95	0.14	1.40	0.02	4.0	5.7	0.40	9.96	5286912	5287424		2
HE 750	64.83	0.47	41.00	0.50	14.58	0.10	2.04	0.02	−14.4	10.5	0.40	9.96	5287680	5288192		
HE 767	62.88	0.45	39.80	0.49	14.11	0.09	1.66	0.02	−0.0	6.6	0.40	9.96	5288448	5288960		
HE 848	115.60	0.83	72.57	0.89	25.57	0.23	4.60	0.04	−7.9	11.7	0.10	9.96	5289216	5289728		
HE 935	123.07	0.89	78.43	0.96	28.01	0.18	3.37	0.03	−8.8	9.1	0.10	9.96	5289984	5290496		
HE 1101	56.66	0.41	35.34	0.43	12.88	0.09	1.50	0.02	−9.7	10.3	0.40	9.96	5290752	5291264		
HE 1234	76.28	0.55	47.58	0.58	16.99	0.11	1.96	0.02	−9.7	17.2	0.40	9.96	5291520	5292032		
HII 120	67.09	0.48	42.19	0.52	15.18	0.10	1.80	0.03	−11.4	16.5	0.40	9.96	5327360	5327872		2
HII 152	67.45	0.49	42.40	0.52	15.16	0.10	2.42	0.03	12.3	14.1	0.40	9.96	6601984	6600192		
HII 173	86.27	0.62	53.77	0.66	19.61	0.13	2.33	0.03	−5.0	11.0	0.40	9.96	5315072	5315584		
HII 174	54.74	0.39	34.10	0.42	12.48	0.08	1.50	0.03	4.9	11.6	0.40	9.96	5315840	5316352		
HII 250	69.23	0.50	44.33	0.54	15.83	0.10	2.12	0.03	4.3	12.2	0.40	9.96	5316608	5317120		
HII 314	80.46	0.58	50.32	0.61	18.23	0.12	2.24	0.03	3.2	14.3	0.40	9.96	5314304	5314816		
HII 514	70.16	0.51	44.24	0.54	15.99	0.11	2.34	0.03	9.8	9.3	0.40	9.96	5317376	5317888		
HII 1015	74.81	0.54	47.49	0.58	16.95	0.11	2.02	0.03	−24.6	11.4	0.40	9.96	5318912	5319424		
HII 1101	91.63	0.66	58.04	0.71	20.89	0.14	3.78	0.03	18.0	14.1	0.40	9.96	6601728	6599936		
HII 1182	77.97	0.56	48.91	0.60	17.49	0.12	2.10	0.03	−4.1	5.4	0.40	9.96	5319680	5320192		

TABLE 1—*Continued*

Source	IRAC 3.6 μm S_ν (mJy)	IRAC 3.6 μm σ_{int} (mJy)	IRAC 4.5 μm S_ν (mJy)	IRAC 4.5 μm σ_{int} (mJy)	IRAC 8 μm S_ν (mJy)	IRAC 8 μm σ_{int} (mJy)	MIPS 24 μm S_ν (mJy)	MIPS 24 μm σ_{int} (mJy)	MIPS 70 μm S_ν (mJy)	MIPS 70 μm σ_{int} (mJy)	IRAC Frame Time (s)	MIPS 24μm DCE Time (s)	AOR Key IRAC	AOR Key MIPS	Flags[a] IRAC	Flags[a] MIPS
HII 1200	112.26	0.81	71.86	0.88	25.02	0.17	3.43	0.03	−22.2	15.6	0.10	9.96	5325824	5326336		
HII 1776	62.92	0.45	39.69	0.48	14.42	0.10	1.75	0.03	−6.1	11.1	0.40	9.96	5328128	5328640		
HII 2147	108.24	0.78	67.89	0.83	24.55	0.17	2.98	0.03	−4.5	5.7	0.10	9.96	5305344	5305856		
HII 2278	91.16	0.66	56.95	0.69	20.87	0.14	2.49	0.03	−14.9	9.9	0.40	9.96	5321216	5321728		
HII 2506	85.60	0.62	54.11	0.66	19.23	0.13	2.33	0.03	5.7	4.6	0.40	9.96	5321984	5322496		
HII 2644	54.39	0.39	33.97	0.41	12.22	0.08	1.43	0.03	3.8	6.6	0.40	9.96	5328896	5329408		
HII 2786	83.50	0.64	53.36	0.65	18.84	0.12	2.20	0.03	2.0	9.8	0.40	9.96	5322752	5323264		
HII 2881	68.28	0.49	43.24	0.53	15.74	0.10	1.78	0.03	8.1	5.9	0.40	9.96	5323520	5324032		
HII 3097	67.41	0.48	42.31	0.52	15.13	0.10	1.84	0.03	−5.7	4.9	0.40	9.96	5324288	5324800		
HII 3179	101.55	0.73	64.27	0.78	22.48	0.15	2.70	0.03	−3.7	3.9	0.10	9.96	5325056	5325568		
HIP 6276	676.70	4.87	418.39	5.10	154.80	1.79	19.26	0.17	13.7	10.6	0.02	2.62	5345792	5346304		
HIP 42491	705.78	5.08	431.44	5.26	157.50	1.53	17.63	0.16	−8.1	11.9	0.02	2.62	5409536	5435904		
HIP 59154	484.75	3.49	294.26	3.59	110.98	0.99	12.92	0.12	0.9	6.0	0.02	2.62	5360384	5360896		
HIP 76477	154.54	1.11	96.58	1.18	35.86	0.24	4.35	0.04	−0.9	8.8	0.10	9.96	5210624	5211136		
MML 1	228.93	1.65	142.01	1.73	52.77	0.35	6.64	0.07	3.3	6.1	0.10	2.62	5240576	5241088		
MML 8	167.52	1.21	104.59	1.28	38.44	0.25	7.81	0.07	17.8	12.9	0.10	9.96	5238272	5238784		
MML 9	165.99	1.20	103.17	1.26	37.89	0.25	4.79	0.04	−6.2	6.7	0.10	9.96	5237504	5238016		
MML 17	228.11	1.64	145.00	1.77	52.24	0.34	9.85	0.09	18.0	7.6	0.10	2.62	5232128	5232640		
MML 18	147.31	1.06	91.80	1.12	33.81	0.22	3.95	0.04	−7.4	11.4	0.10	9.96	5277696	5278208		
MML 26	138.07	0.99	86.42	1.05	31.47	0.24	3.72	0.03	−1.6	8.1	0.10	9.96	5230592	5231104	1	
MML 28	92.92	0.67	57.95	0.71	21.45	0.14	3.55	0.03	10.1	10.1	0.40	9.96	5276928	5277440		
MML 32	132.67	0.95	84.46	1.03	30.41	0.20	3.72	0.03	6.4	12.0	0.10	9.96	5235968	5236480		
MML 36	216.06	1.56	135.16	1.79	49.64	0.33	8.95	0.08	3.9	4.1	0.10	9.96	5235200	5235712		
MML 38	108.23	0.78	68.47	0.83	24.83	0.16	3.12	0.03	−1.0	5.9	0.10	9.96	5233664	5234176		
MML 40	124.46	0.90	78.01	0.95	28.80	0.19	3.48	0.03	−3.2	4.5	0.10	9.96	5239808	5240320		
MML 43	116.39	0.84	73.09	0.89	26.79	0.18	3.62	0.03	−7.6	8.0	0.10	9.96	5232896	5233408		
MML 51	146.14	1.05	92.99	1.14	34.52	0.23	4.17	0.04	2.0	3.7	0.10	9.96	5212160	5212672		
MML 57	118.05	0.85	74.25	0.91	26.93	0.18	3.55	0.03	7.7	12.7	0.10	9.96	5229824	5230336		
PDS 66	656.79	4.73	521.43	6.36	470.62	3.11	1874	94	1672.0	14.9	0.02	2.62	5198080	5198592		
[PZ99] J155847.8−175800	147.12	1.06	93.15	1.14	35.28	0.23	6.11	0.06	−21.8	14.8	0.40	9.96	5202944	5203456		
[PZ99] J160814.7−190833	135.31	0.97	84.71	1.03	31.66	0.23	3.74	0.04	6.4	13.2	0.10	9.96	5249792	5250304		
[PZ99] J161318.6−221248	325.68	2.35	204.71	2.50	76.83	0.51	9.14	0.09	−20.8	12.1	0.10	2.62	5203712	5204224		
[PZ99] J161329.3−231106	139.25	1.00	87.83	1.07	33.38	0.23	4.12	0.04	12.7	11.1	0.10	9.96	5204480	5204992	1	
[PZ99] J161402.1−230101	119.64	0.86	75.34	0.92	28.25	0.19	3.66	0.04	−19.6	13.0	0.10	9.96	5205248	5205760		
[PZ99] J161411.0−230536	498.31	3.59	401.87	4.90	363.52	2.40	304.0	2.7	91.1	11.7	0.02	2.62	5206016	5206528		
[PZ99] J161459.2−275023	101.69	0.73	63.27	0.77	23.80	0.16	4.53	0.04	26.6	25.0	0.10	9.96	5219072	5219584		
[PZ99] J161618.0−233947	170.49	1.23	106.52	1.30	40.09	0.27	5.35	0.05	−14.8	14.0	0.10	9.96	5219840	5220352		
QT And	324.14	2.33	204.36	2.49	76.23	0.50	9.12	0.08	−8.4	5.8	0.10	2.62	5299200	5299712		2
R3	58.19	0.42	36.27	0.59	13.34	0.09	1.52	0.02	−10.5	9.0	0.40	9.96	5272320	5272832		
R45	63.91	0.46	40.38	0.49	14.43	0.10	1.90	0.02	2.3	21.4	0.40	9.96	5273856	5274368		2
R83	68.66	0.49	43.22	0.53	15.61	0.10	1.80	0.02	−24.7	12.8	0.40	9.96	5273088	5273600		
RE J0137+18A	662.72	9.43	413.67	5.05	151.77	1.00	17.50	0.16	2.7	4.5	0.02	2.62	5242112	5242624	1	
RE J0723+20	545.19	3.92	338.81	4.13	125.47	0.83	15.26	0.14	1.0	5.0	0.02	2.62	5348096	5348608		
RX J0258.4+2947	71.67	0.52	44.92	0.55	16.40	0.11	1.92	0.02	−5.3	4.0	0.40	9.96	5358080	5358592		

TABLE 1—*Continued*

Source	IRAC 3.6 μm S_ν (mJy)	IRAC 3.6 μm σ_{int} (mJy)	IRAC 4.5 μm S_ν (mJy)	IRAC 4.5 μm σ_{int} (mJy)	IRAC 8 μm S_ν (mJy)	IRAC 8 μm σ_{int} (mJy)	MIPS 24 μm S_ν (mJy)	MIPS 24 μm σ_{int} (mJy)	MIPS 70 μm S_ν (mJy)	MIPS 70 μm σ_{int} (mJy)	IRAC Frame Time (s)	MIPS 24μm DCE Time (s)	AOR Key IRAC	AOR Key MIPS	Flags[a] IRAC	Flags[a] MIPS
RX J0329.1+0118	63.93	0.46	40.80	0.50	14.68	0.10	1.71	0.02	2.1	4.8	0.40	9.96	5352704	5353216	1	
RX J0331.1+0713	179.78	1.29	112.98	1.38	42.16	0.28	4.94	0.04	−4.7	5.3	0.10	9.96	5242880	5243392	1	
RX J0354.4+0535	103.00	0.74	65.35	0.80	23.61	0.18	3.09	0.03	−7.2	5.0	0.10	9.96	5299968	5300480		
RX J0357.3+1258	77.05	0.56	48.40	0.59	17.72	0.12	2.20	0.03	−3.3	5.7	0.40	9.96	5256192	5256704		
RX J0434.3+0226	48.51	0.35	31.07	0.38	11.46	0.08	1.38	0.02	−5.9	4.1	0.40	9.96	5300736	5301248	1	2
RX J0442.5+0906	67.02	0.48	41.52	0.51	15.23	0.10	1.75	0.03	1.2	4.5	0.40	9.96	5304576	5305088		
RX J0849.2−7735	1444.48	10.40	881.70	10.76	336.69	2.22	39.20	0.35	3.1	8.0	0.02	2.62	5312768	5313280		
RX J0850.1−7554	98.81	0.71	61.45	0.75	22.27	0.15	2.78	0.03	3.3	3.5	0.10	9.96	5298432	5298944		
RX J0853.1−8244	72.44	0.52	45.83	0.56	17.03	0.11	2.05	0.02	−5.3	3.3	0.40	9.96	5351168	5351680		
RX J0917.2−7744	91.21	0.66	57.60	0.70	20.83	0.14	2.38	0.02	3.1	3.3	0.40	9.96	5351936	5352448		2
RX J1111.7−7620	447.93	3.23	363.46	4.43	198.69	1.86	229.6	2.1	224.3	8.3	0.02	2.62	5199616	5200128		2
RX J1140.3−8321	114.19	0.82	69.97	0.85	26.43	0.17	3.02	0.03	−2.0	5.0	0.10	9.96	5260800	5261312		
RX J1203.7−8129	71.75	0.52	45.29	0.55	16.61	0.11	1.99	0.02	2.6	4.7	0.40	9.96	5354240	5354752		
RX J1209.8−7344	163.91	1.18	102.40	1.25	38.64	0.26	4.62	0.04	−4.4	5.0	0.10	9.96	5361152	5361664		
RX J1220.6−7539	200.62	1.45	124.54	1.52	46.07	0.30	5.48	0.05	−12.4	4.3	0.10	9.96	5355008	5355520		2
RX J1225.3−7857	112.89	0.81	70.60	0.86	25.73	0.17	3.05	0.03	−0.9	3.9	0.10	9.96	5355776	5356288		
RX J1450.4−3507	178.29	1.28	112.17	1.37	41.31	0.27	4.91	0.04	−3.7	4.0	0.10	9.96	5214464	5214976		
RX J1457.3−3613	149.56	1.08	94.73	1.16	34.38	0.23	4.32	0.04	−1.2	5.4	0.10	9.96	5225984	5226496		
RX J1458.6−3541	211.96	1.53	133.68	1.63	49.73	0.33	5.97	0.05	7.6	4.2	0.10	9.96	5211392	5211904		
RX J1500.8−4331	96.40	0.69	61.33	0.75	22.54	0.15	2.65	0.02	−10.0	8.2	0.40	9.96	5264640	5265152		
RX J1507.2−3505	137.35	0.99	85.39	1.04	31.64	0.21	4.05	0.04	−0.1	6.1	0.10	9.96	5270784	5271296		
RX J1518.4−3738	121.24	0.87	77.05	0.94	28.29	0.19	3.48	0.04	−1.8	5.8	0.10	9.96	5281536	5282048		
RX J1531.3−3329	95.38	0.69	59.77	0.73	21.97	0.14	2.49	0.04	12.4	13.1	0.40	9.96	5280000	5280512		
RX J1541.1−2656	82.17	0.59	51.08	0.62	19.05	0.13	2.27	0.03	−37.2	13.3	0.40	9.96	5202176	5202688		
RX J1544.0−3311	138.34	1.00	87.01	1.06	32.21	0.21	4.04	0.04	−22.4	12.0	0.10	9.96	5279232	5279744	1	
RX J1545.9−4222	209.09	1.50	131.65	1.61	49.24	0.33	5.83	0.07	−27.9	12.6	0.10	2.62	5215232	5215744		
RX J1600.6−2159	134.55	0.97	85.17	1.04	31.42	0.21	4.38	0.04	9.9	15.7	0.10	9.96	5253376	5253888		
RX J1839.0−3726	112.27	0.81	70.86	0.86	25.95	0.17	3.39	0.04	−7.6	7.2	0.10	9.96	5223680	5224192		
RX J1841.8−3525	187.75	1.35	119.45	1.46	43.02	0.28	5.37	0.05	−1.7	5.3	0.10	9.96	5216768	5217280		
RX J1842.9−3532	269.53	1.94	216.15	2.64	157.35	1.04	358.9	3.2	942.6	13.8	0.10	2.62	5198848	5199360		
RX J1844.3−3541	141.52	1.02	88.66	1.08	32.65	0.22	3.84	0.04	−17.9	6.5	0.10	9.96	5249024	5249536		
RX J1852.3−3700	88.58	0.64	58.49	2.04	33.64	0.97	472.2	4.2	1367.0	14.6	0.02	2.62	5200384	5200896		
RX J1917.4−3756	318.64	2.29	198.72	2.42	73.67	0.49	8.82	0.08	2.1	6.9	0.10	2.62	5209088	5209600		
RX J2313.0+2345	107.93	0.78	67.33	0.82	24.13	0.23	2.80	0.03	−3.3	4.4	0.10	9.96	5243648	5244160	1	2
SAO 150676	306.12	2.20	191.84	2.34	70.27	0.46	8.72	0.08	2.1	4.3	0.10	2.62	5294592	5295104		
SAO 178272	327.04	2.35	203.57	2.48	75.43	0.50	9.08	0.08	1.5	3.5	0.10	2.62	5309696	5310208		
ScoPMS 21	120.69	0.87	76.08	0.93	28.71	0.19	3.62	0.06	−8.1	26.1	0.10	9.96	5201152	5201664		
ScoPMS 27	186.26	1.34	116.92	1.43	43.94	0.29	5.25	0.08	7.3	11.4	0.10	2.62	5196544	5197056		
ScoPMS 52	319.90	2.30	200.77	2.45	75.93	0.50	8.89	0.11	34.5	23.8	0.10	2.62	5217536	5218048		
ScoPMS 214	242.00	1.74	154.41	1.88	59.07	0.39	7.75	0.14	15.1	15.4	0.60	2.62	5672448	5706496	3	4
V343 Nor	1344.03	9.68	846.43	10.33	308.70	2.04	36.77	0.33	−1.3	40.0	0.02	2.62	5222912	5223424		
V383 Lac	752.12	5.42	466.84	5.70	170.11	1.33	20.27	0.18	7.8	8.6	0.02	2.62	5296128	5296640		
W79	42.02	0.30	26.01	0.32	9.52	0.06	1.38	0.02	0.2	13.7	0.40	9.96	5274624	5275136		
vB 1	1157.67	8.34	733.56	8.95	259.47	1.71	28.51	0.26	14.1	12.2	0.02	2.62	5403392	5403904	1	

TABLE 1—*Continued*

Source	IRAC						MIPS				IRAC Frame Time (s)	MIPS 24μm DCE Time (s)	AOR Key		Flags[a]	
	3.6 μm		4.5 μm		8 μm		24 μm		70 μm							
	S_ν (mJy)	$\sigma_{\rm int}$ (mJy)	S_ν (mJy)	$\sigma_{\rm int}$ (mJy)	S_ν (mJy)	$\sigma_{\rm int}$ (mJy)	S_ν (mJy)	$\sigma_{\rm int}$ (mJy)	S_ν (mJy)	$\sigma_{\rm int}$ (mJy)			IRAC	MIPS	IRAC	MIPS
vB 39	907.63	6.54	581.32	7.09	214.07	1.95	24.26	0.22	−3.5	10.3	0.60	2.62	4096512	5376256	3	
vB 49	531.47	3.83	333.05	5.62	123.24	1.12	13.61	0.12	−5.8	7.7	0.60	2.62	4096512	5376768	3	
vB 52	856.95	6.17	545.70	6.66	200.27	1.32	22.48	0.20	0.6	10.6	0.60	2.62	4096512	5377280	3	
vB 63	750.87	6.02	480.71	5.87	177.66	1.52	19.97	0.18	3.0	10.7	0.60	2.62	4096512	5377792	3	
vB 64	658.77	4.78	422.85	5.16	152.25	1.00	16.96	0.15	−4.3	11.8	0.60	2.62	4096512	5378304	3	
vB 66	961.97	6.93	609.26	7.43	216.22	1.43	24.58	0.22	10.2	11.4	0.02	2.62	5367552	5368064		
vB 73	756.94	5.45	476.39	5.81	176.50	1.17	20.16	0.18	−8.4	10.4	0.60	2.62	4096512	5378816	3	
vB 79	422.74	3.14	266.31	4.12	99.03	1.03	10.95	0.10	−7.6	7.9	0.60	2.62	4096512	5379328	3	
vB 88	741.40	5.34	469.92	5.73	165.43	1.09	18.93	0.17	−11.3	12.5	0.02	2.62	5397248	5397760		
vB 91	574.70	4.14	349.43	4.26	131.46	0.87	14.81	0.13	−9.3	12.7	0.60	2.62	4096768	5379840	3	
vB 92	473.38	6.60	291.35	4.07	109.07	0.94	12.07	0.11	−2.6	13.8	0.60	2.62	4096768	5380352	3	
vB 93	330.46	2.38	204.75	2.50	76.29	0.50	8.42	0.08	7.5	8.4	0.60	2.62	4096768	5380864	3	
vB 96	722.91	7.20	449.19	5.48	167.82	1.11	18.54	0.17	−13.6	12.3	0.60	2.62	4096768	5381376	3	
vB 97	730.07	10.70	462.11	5.64	169.52	1.12	19.07	0.17	−5.3	12.0	0.60	2.62	4096768	5381888	3	2
vB 99	314.03	2.26	197.40	2.41	73.14	0.48	8.19	0.08	−4.7	12.1	0.60	2.62	4096768	5382400	3	
vB 106	770.31	5.55	479.30	5.85	171.24	1.13	19.42	0.17	10.3	11.5	0.02	2.62	5392640	5393152		
vB 142	572.80	4.12	354.86	4.33	128.34	2.14	14.38	0.13	2.2	11.9	0.02	2.62	5329664	5330176		
vB 143	626.50	4.51	391.13	4.77	139.51	0.92	15.68	0.14	−4.8	11.3	0.02	2.62	5406464	5406976		
vB 176	550.88	7.35	337.21	4.11	128.40	0.95	14.26	0.13	−0.6	7.2	0.60	2.62	4096512	5382912	3	
vB 180	404.68	2.91	251.91	3.07	94.00	1.25	10.52	0.09	2.4	7.1	0.60	2.62	4096768	5383424	3	
vB 183	266.16	1.92	168.22	2.05	63.01	0.43	7.04	0.08	−11.7	12.4	0.60	2.62	4096768	5383936	3	

[a] Comments: (1) IRAC photometry performed using aperture radius of 4 pixels. (2) Neighboring source subtracted from MIPS 70 μm image before measuring photometry. (3) IRAC photometry measured using non-FEPS, archival data. (4) MIPS photometry measured using non-FEPS, archival data.

source were observed in all four IRAC bands for the initial verification observations. The IRAC 5.8 μm observations were dropped for the remaining sources since it had the lowest S/N of the four IRAC bands. The IRAC 5.8 μm data are described in Meyer et al. (2004) and are not further discussed here.

Four-band IRAC GTO observations of the 16 Hyades stars and c2d observations of ScoPMS 214 were observed in full-array, high-dynamic-range mode, where an image is obtained with a 0.6 s frame time followed by an image with a 12 s frame time. The Hyades stars were observed at three dither positions, and ScoPMS 214 at two positions in this manner. The 12 s frame-time images in IRAC 3.6, 4.5, and 5.8 μm bands were saturated and not analyzed.

2.1. *Image Processing*

Analysis was performed on Basic Calibrated Data (BCD) products generated by the data reduction pipeline version S13 developed at the *Spitzer* Science Center (SSC). The SSC pipeline removes the electronic bias, subtracts a dark image, applies a flat-field correction, and linearizes the pixel response. Additional processing on the BCD images was performed by the FEPS team as now described.

For the subarray data, cosmic-ray hits were identified and flagged by filtering the sequence of 64 frames at each dither position. At a given pixel, the median and standard deviation of the 64 frames values were computed from the median absolute deviation[9] to reduce sensitivity to outlier pixel values. Any pixels that deviated from the median by more than $n\sigma$ were flagged, where n was calculated to correspond to a probability of 10^{-4} that such an outlier pixel could occur by Gaussian noise given N images (nominally, $N = 64$ and $n \approx 4.8$). For 26 frames (or 0.03% of the data), the rejected pixel was within the photometric aperture and the entire frame was discarded. The median and dispersion were recomputed in an iterative fashion until no additional pixels were flagged. For sources HD 77407 and HD 70516, we removed all frames at two dither positions where the FEPS target position overlapped with a latent image.

For the archival full-array observations, cosmic-ray rejection was performed by the MOPEX[10] (Makovoz & Marleau 2005) mosaicking package. Images were aligned spatially based on the World Coordinate Systems (WCS) parameters in the image headers. The standard deviation at each pixel position in the stack of aligned images was computed from the median absolute deviation. Pixel values that deviated more than 5 σ from the median were removed.

After outlier rejection, both the sub- and full-array images were multiplied by the photometric correction images produced by the SSC that account for variations in the pixel solid angle and the effective response of the filters across the IRAC focal plane.[11] These correction images were derived by observing a star at 225 positions across the full array and thus link the calibration of sub- and full-array observations.

2.2. *Photometry*

IRAC photometry was measured with a modified version of IDLPHOT.[12] We measured source flux densities with aperture photometry instead of point-response-function (PRF) fitting photometry since the PRF is undersampled in the IRAC 3.6 μm band and the PRF shape depends on the position of the star within a pixel. Aperture photometry was performed on each frame with an aperture radius of 3 pixels. This aperture size was chosen as a compromise between S/N (which empirically was highest for an aperture radius of 2 pixels) and obtaining accurate calibration between full and subarray observations (which favored larger apertures to reduce the effects of image distortion). The sky background was computed in an annulus on the source centroid with an inner radius of 10 pixels and a width of 10 pixels so that the aperture corrections can be compared directly to values listed in the *Spitzer* Observing Manual.[13] Pixel values in the sky annulus were sigma-clipped in an iterative fashion with a clipping threshold of 3 σ, where the dispersion in the sky background was estimated from the median absolute deviation. The sky value was estimated as the mean of the remaining pixels. For several sources, the S/N was too low to derive an accurate centroid on individual frames. A subset of frames was then co-added until the formal, internal positional uncertainty was less than 0.1 pixels.

In the IRAC 3.6 μm band, the measured flux density can vary up to 3.6% depending on the distance of the centroid position from the pixel center (Reach et al. 2005), which is defined as the pixel phase (p). This dependency may be caused by nonuniform quantum efficiency across a pixel. The best-fit correction factor ($f_{\rm phase}$) derived from the FEPS data is $f_{\rm phase} = 1.0232–0.0582p$, which is similar to that obtained by Reach et al. (2005). A correlation of similar magnitude between intensity and pixel phase was found for only one of the four dither positions in the 4.5 μm band, and none of the dither positions in the 8 μm band. Pixel phase corrections were applied on individual images for the IRAC 3.6 μm band only using the above relation.

Aperture corrections are needed to convert the photometry to the fiducial 10 pixel aperture used to calibrate the IRAC instrument (Reach et al. 2005). The multiplicative scaling factor for the 3 pixel aperture was measured from the FEPS data by computing the ratio of the flux density in a 10 pixel aperture to that in a 3 pixel aperture. The derived aperture corrections for a 3 pixel wide aperture are 1.109, 1.110, and 1.200 for IRAC bands 3.6, 4.5, and 8 μm, respectively. These aperture corrections agree with the values listed on the SSC IRAC Data Handbook[14] to within 0.3% for the 3.6 and 4.5 μm bands, and 1.5% for the 8 μm band. The measured aperture corrections for 23 sources deviated by more than 3 σ from the nominal value. Twenty of these sources are known from an adaptive optics survey to be multiple systems with a separation of $\lesssim 2''$ between the primary and secondary components (S. Metchev 2007, private communication). The other three sources have not been observed at high resolution and the multiplicity status is unknown. For these 23 stars, the measured aperture correction at a four pixel radius is within 1.3% of the nominal correction for each source, and a four pixel aperture radius was used with aperture corrections of 1.069, 1.079, and 1.081 for IRAC bands 3.6, 4.5, and 8 μm, respectively. These stars are noted in Table 1.

Flux densities were computed as the unweighted average of the flux densities measured in N dither positions ($N = 4$ nominally). The standard deviation of the N dither positions ($\equiv\sigma_{\rm rms}$), normalized by the mean flux density, is plotted versus the mean flux density in Figure 1. For the IRAC 3.6 and 4.5 μm bands, the normalized rms shows no trend with mean flux density, while for IRAC 8 μm, the normalized rms increases systematically toward

[9] The median absolute deviation (MAD) is defined as MAD = median$_i$($|x_i -$ median$_j(x_j)|$) (Hampel 1974). The standard deviation is estimated from the MAD as $\sigma \approx 1.4826$ MAD.

[10] See http://ssc.spitzer.caltech.edu/postbcd.

[11] The correction images are available at http://ssc.spitzer.caltech.edu/irac/calib.

[12] See http://idlastro.gsfc.nasa.gov.

[13] See http://ssc.spitzer.caltech.edu/documents/SOM.

[14] See http://ssc.spitzer.caltech.edu/irac/dh.

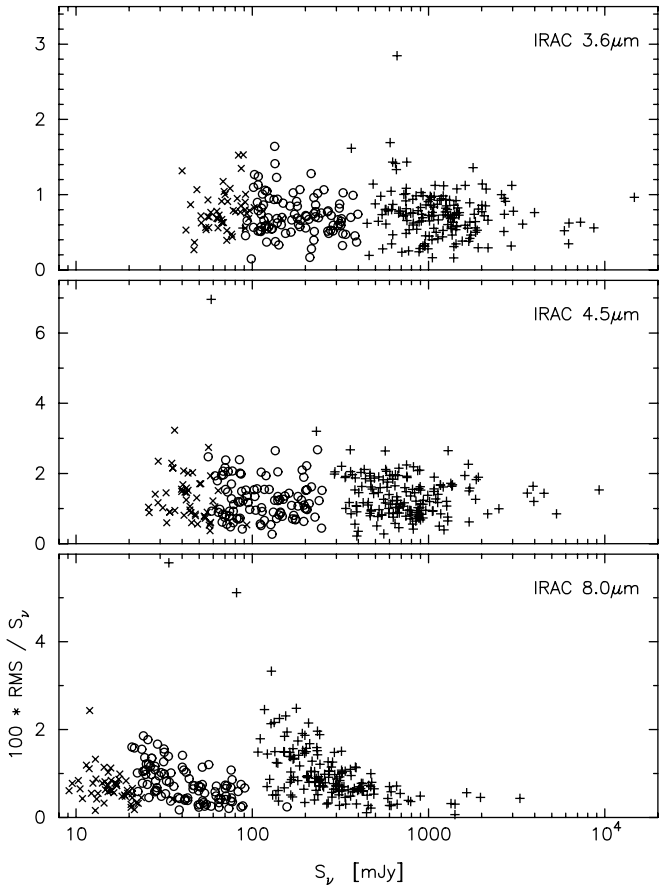

FIG. 1.—Normalized rms of the measured flux densities in the four subarray dither positions plotted vs. the mean flux density for the FEPS IRAC subarray observations. Stars observed with IRAC frame times of 0.02, 0.1, and 0.4 s are represented by plus signs, open circles, and times signs, respectively. We used the repeatability between the dithered observations to assign a minimum photometric uncertainty of 0.72%, 1.22%, and 0.66% for IRAC bands 3.6, 4.5, and 8 μm, respectively.

fainter sources for a fixed frame time. This trend is expected if the S/N is photon limited and the integration time is constant since fainter sources will have lower S/N. The photometric repeatability at a fixed dither position indicates that the standard deviation of the photometry computed from the four dither positions should be $<0.4\%$ in each band for the brighter stars. Given that the repeatability between dithers is poorer, the photometric precision is limited by either our data reduction procedures or instrumental limitations in obtaining dithered data. Internal photometric uncertainties were therefore computed as $\sigma_{\rm rms}/\sqrt{N}$, but with a minimum uncertainty imposed. For the IRAC 3.6 and 4.5 μm bands, we adopt a minimum internal uncertainty of 0.72% and 1.22%, respectively, which corresponds to the median repeatability from the ensemble data shown in Figure 1. For the IRAC 8 μm band, we adopt a minimum uncertainty of 0.66%, which is the median value for stars with a repeatability less than 1.2%.

We investigated the relative calibration of IRAC sub- and full-array data since the flux calibrators used by Reach et al. (2005) were observed in full-array mode. To compare the subarray and full-array calibration, we analyzed observations of the star HD 135285 that were obtained by the SSC in full-array mode and in subarray mode with 0.4 s integration times. The mean ratio of the flux densities measured in subarray mode to that in full-array mode is 1.004 ± 0.004 for the IRAC 3.6 μm band, 1.001 ± 0.004 for 4.5 μm, 0.995 ± 0.002 for 5.8 μm, and 0.997 ± 0.001 for 8 μm. The weighted mean for all four bands is 0.997 ± 0.001. We conclude that any calibration offsets between the 0.4 s subarray mode and full-array mode is less than 1%, and no further calibration corrections were applied to the subarray observations. In § 7 we consider the relative subarray calibration for the different frame times.

The IRAC photometry and internal uncertainties are presented in Table 1. The flux density measurements are tied to the calibration described in Reach et al. (2005) with calibration factors of 0.0188, 0.1388, and 0.2021 MJy sr^{-1} per DN s^{-1} for IRAC 3.6, 4.5, and 8 μm, respectively, and a 1 σ uncertainty of 2%.

3. MIPS 24 μm

The MIPS instrument obtains images in the 24, 70, and 160 μm bands. This section describes the data reduction procedures for the 24 μm band. The 70 μm data are discussed in § 4, and analysis of the 160 μm data are presented in Kim et al. (in preparation). The 128×128 pixel MIPS 24 μm array images an instantaneous field of view of $\sim 5.4' \times 5.4'$ region with a pixel scale of $2.5'' \times 2.6''$. The FEPS team obtained MIPS 24 μm observations in photometry mode for 323 sources. Data for five stars (HD 17925, HD 72905, HD 202917, HD 216803, ScoPMS 214) were extracted from the *Spitzer* archive. The exposure time (either 3 or 10 s) and the number of dithered images (either 28 or 56) were set to achieve a signal to noise of at least 30 on the expected stellar photosphere brightness.

3.1. *Image Processing*

MIPS 24 μm images for all but one source were processed with SSC pipeline version S13. The star HD 143006 has a flux density of $\sim$3 Jy at 24 μm, and S13 data products have an error in the linearity correction for such bright sources. For HD 143006 only, we used S16 data products where the linearity problem was fixed.

Individual BCD images that contain the "strong" jailbar effect caused by bright sources or cosmic rays were removed on visual inspection. Images were also removed if cosmic-ray hits were found near the expected source position. These images were identified by performing aperture photometry on individual BCD images, and finding outlier flux densities or centroid coordinates compared to the mean that had less than a 10^{-4} chance to have been caused by random noise.

Once contaminated BCD images were removed, additional processing steps were performed following the recommendations from the SSC MIPS handbook and the MIPS instrument team (Engelbracht et al. 2007). First, for a given source, background levels in individual images were adjusted to a common median value using an additive constant. Images for a given source were then median combined to derive a flat-field image which removes long-term gain changes in the MIPS array. For the median filtering, a 5 pixel radius region centered on the source position was masked. A 3 σ clipping algorithm was used to remove outliers on a pixel-by-pixel basis through the image stack. The resulting median image was normalized by the median pixel value over the image. Flat-field images were derived only for sources that are not surrounded by nebulosity. Affected sources were identified from visual inspection of the image mosaics. If nebulosity is present, a flat-field image from another FEPS source was used that was (1) obtained within a time interval ± 1 day, (2) had the same exposure time, and (3) had the closest matched background level. If no such image existed, the image nearest in time with the same exposure time was used. The stability of the flats over time were assessed by taking the ratio of flats taken on different days. Over a ± 3 day period, the mean flat-field value

for the central 5×5 pixel region of the MIPS 24 μm array is repeatable to 1.4% peak-to-peak with a dispersion of 0.2%.

3.2. *Photometry*

Photometry was performed with the MOPEX package (Makovoz & Marleau 2005). The BCD images for a given source were aligned spatially based on the WCS information in the image headers. Cosmic-ray rejection was performed by removing pixels within the stack that deviated by more than 5 σ from the mean. Point sources were identified on a mosaic of the BCD images using a 10 σ detection threshold. The detection list was modified after visual inspection of the mosaics to remove spurious sources and to add any sources missed by the automated detection method.

PRF fitting photometry was performed with the APEX module in MOPEX. PRF fitting photometry was chosen over aperture photometry since the PRF is critically sampled in the MIPS 24 μm images and should provide the optimum signal to noise. The empirical PRF distributed with the APEX package was fitted to the individual BCD images simultaneously (as opposed to the mosaicked image) using a fitting area of 21×21 pixels for most images. A 5×5 pixel fitting area was used for 11 sources that have spatially variable nebulosity near the point source position. From visual inspection of the mosaicked images, the PRF from other 24 μm sources sometimes overlapped with the PRF from the FEPS target. These contaminating sources were fitted with a PRF simultaneously with the FEPS target. The free parameters in the PRF fit include a spatially constant sky background level, and the peak flux density and centroid position for each source.

Photometry was measured by integrating the fitted PRF within a 3 pixel radius (1 pixel $\sim$2.55″) since the wings of the PRF have lower signal to noise. An aperture correction is then needed to place the PRF photometry on the zero-point scale adopted by the MIPS instrument team. The aperture correction was derived by measuring aperture photometry on individual BCD images using a customized version of IDLPHOT. We adopted an aperture radius of 13″ and a sky annulus between 20″ and 32″ since these aperture parameters have been calibrated by the MIPS instrument team to a theoretical PRF. Aperture flux densities were computed as the unweighted mean of the photometry measured on individual BCD images. The average ratio of the flux density measured with 13″ aperture photometry compared to 3 pixel (7.65″) PRF photometry is 1.371 with a dispersion of 0.011 for 108 sources brighter than 20 mJy. From the SSC World Wide Web site,[15] the aperture correction for a 13″ aperture radius and the adopted sky annulus is a 1.167. The final flux densities were obtain by multiplying the PRF flux densities by the product of these factors (1.600).

Internal uncertainties computed by APEX are often much smaller ($\ll$1%) than is assessed from repeated observations of the source. The minimum internal uncertainty was estimated based on photometric repeatability from aperture photometry. The normalized rms of the MIPS 24 μm flux densities measured from *aperture* photometry on individual BCD images is presented in Figure 2. For sources brighter than 100 mJy, the mean rms repeatability is 0.9% in a 3 pixel aperture radius, which we adopted as the minimum uncertainty for the PRF photometric uncertainties.

The MIPS 24 μm photometry and internal uncertainties are presented in Table 1. The S13 images were processed with a calibration factor of 0.0447 MJy sr^{-1}. Following Engelbracht et al. (2007), we adopt a calibration uncertainty of 4%.

[15] See http://ssc.spitzer.caltech.edu/mips/apercorr.

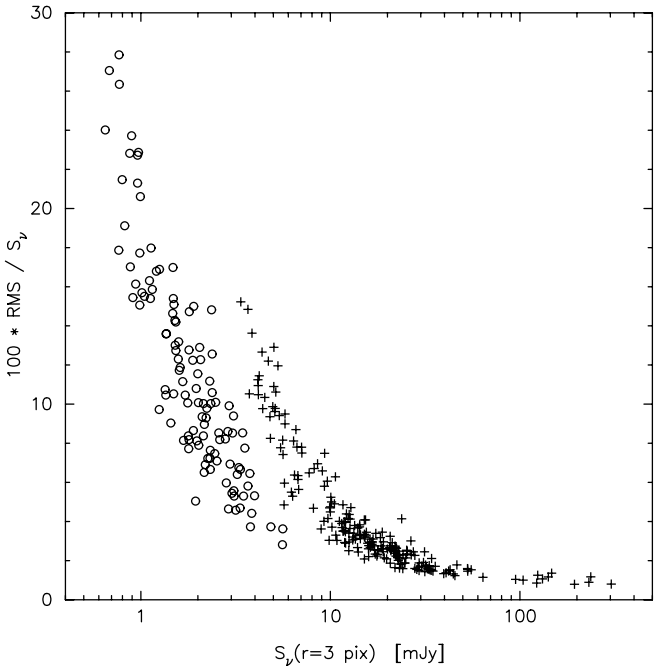

FIG. 2.—Repeatability of the rms of the MIPS 24 μm aperture photometry measured in a 3 pixel radius on individual BCD images. Crosses represent sources observed with an exposure time of 3 s, and open circles with 10 s. We adopted a minimum uncertainty of 0.9% based on the mean repeatability for stars brighter than 100 mJy.

4. MIPS 70 μm

We obtained MIPS 70 μm observations for 323 sources and extracted data for five stars (HD 17925, HD 72905, HD 202917, HD 216803, ScoPMS 214) from the *Spitzer* archive. The FEPS observations were obtained in photometry mode with an exposure time of 10 s and the small field size dither pattern. A single MIPS 70 μm image in this mode contains 32×32 pixels with a scale of 9.8″ pixel^{-1}. The FEPS sources were centered on the left half of the array which had the best sensitivity. The number of cycles per source ranged between 2 and 10, where a cycle contains up to 12 dithered images. The number of cycles were set based on the stellar distance and age to reach the expected brightness of the outer solar system dust level at that stellar age (see Hillenbrand et al. 2008).

4.1. *Image Processing*

MIPS 70 μm images were processed with SSC pipeline version S13 that removes the bias, subtracts a dark image, applies a flat-field correction, and linearizes the pixel response. Individual BCD images were mosaicked with the Germanium Reprocessing Tools (GeRT) software package S14.0 version 1.1 developed at the SSC. The GeRT package performs column spatial filtering on the BCD images and then a time median filter to remove residual pixel response variations. A $40'' \times 40''$ region centered on the source position, compared to the PRF FWHM size of 18″, was excluded when computing the column and time filtering such that the filtering process is not biased by the presence of a bright source. Filtered images were formed into mosaics with MOPEX (Makovoz & Marleau 2005). Outlier pixels were rejected using a 3 σ clipping threshold.

4.2. *Photometry*

Aperture photometry was performed on the MIPS 70 μm mosaics with a custom version of IDLPHOT. We adopted aperture

photometry over PRF fitting photometry since most sources were not detected at 70 μm, and aperture photometry enables a straightforward interpretation of the upper limits.

The adopted aperture radius of 16″ (4 pixels on the co-added images), which corresponds to approximately the FWHM size of the PRF, was chosen to optimize the S/N for faint sources (see, e.g., Naylor 1998). The sky level was computed as the mean pixel value in a sky annulus that extends from 40″ to 60″ after performing the iterative clipping procedure described in § 2.2. The aperture was centered on the expected stellar position computed from the WCS parameters contained in the FITS image headers, and no centroiding was performed. Visual inspection of the 70 μm mosaics identified 19 images where a point source was located within the outer sky annulus or the aperture radius, but offset from the stellar position determined from 2MASS astrometry. A PRF was fitted to the contaminating source and subtracted from the image using MOPEX. These 19 sources are identified in Table 1. Aperture photometry was recomputed on the PRF-subtracted image.

The 70 μm photometric uncertainty was computed as

$$\sigma = (\eta_{\rm sky}\eta_{\rm corr})(\Omega\Sigma_{\rm sky})\sqrt{N_{\rm ap} + N_{\rm ap}^2/N_{\rm sky}}, \quad (1)$$

where $\Sigma_{\rm sky}$ is the noise per pixel in units of surface brightness as measured in the sky annulus, Ω is the solid angle of a pixel, $N_{\rm ap}$ is the number of pixels in the aperture, $N_{\rm sky}$ is the number of pixels in the sky annulus, and $\eta_{\rm sky}$ and $\eta_{\rm corr}$ correct for correlated noise terms as described below. The total uncertainty is the rms sum of two terms: the term proportional to $(N_{\rm ap})^{1/2}$ is the uncertainty from random fluctuations in the pixel noise summed over the aperture, and the term proportional to $(N_{\rm ap}^2/N_{\rm sky})^{1/2}$ represents the uncertainty in the mean pixel noise from the sky annulus (often assumed to be zero due to the large area over which one usually measures the mean sky).

Two correction factors are needed to compute accurate uncertainties. Because the 70 μm mosaics were sampled at a finer scale than the raw images, the noise between adjacent pixels is correlated. The factor $\eta_{\rm corr}$ accounts for the correlated noise, and was estimated as the ratio of the pixel size in the raw images (9.8″) to that in the mosaics (4″), or $\eta_{\rm corr} = 2.5$.

The second correction factor, $\eta_{\rm sky}$, accounts for systematic differences in the pixel noise between the aperture and sky annulus. Variations in the pixel noise as a function of position across the mosaics were assessed by first scaling all 70 μm mosaics in the FEPS program to a common median value. The standard deviation of each pixel in the stack of mosaic images was computed after removing 35 images where the FEPS target was clearly detected. The resulting image showed that the mosaic noise was higher along the columns near the source position due to time-variable latent images from the calibration stim flashes. The pixel noise was estimated to be 40% higher in the aperture compared to the sky annulus, and we adopt $\eta_{\rm sky} = 1.40$.

Figure 3 shows a histogram of the S/N for the 70 μm photometry. Visual inspection of the mosaicked images indicates that the majority of the FEPS sources have not been detected at 70 μm. The histogram in Figure 3 should then be a Gaussian with unit dispersion (Fig. 3, *solid curve*) if equation (1) contains the dominant noise terms. In practice, the observed S/N distribution is broader than the expected Gaussian distribution and includes S/N values as low as -4.2.

As shown by the dotted curve in Figure 3, a Gaussian with a dispersion of 1.49 adequately describes the observed distribution. The origin of the apparent excess noise is unknown, but nonetheless, we have scaled the photometric uncertainties for all sources by a factor of 1.49.

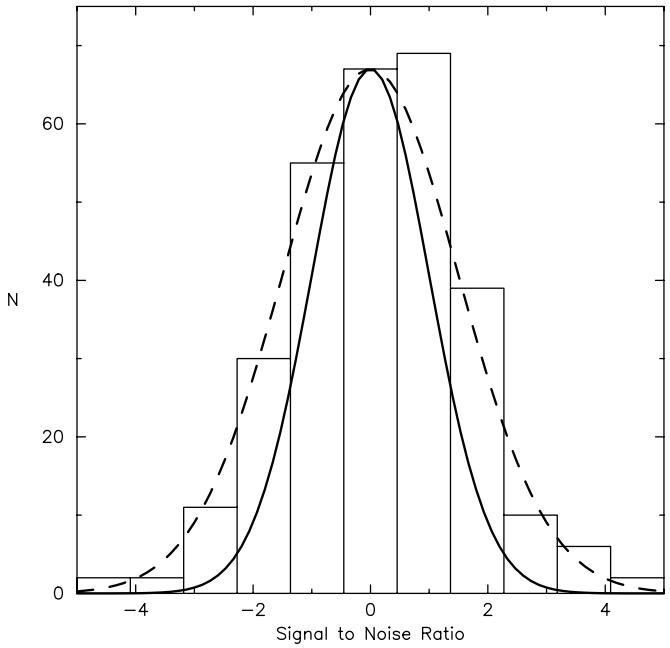

FIG. 3.—Histogram of the S/N measured in a 16″ radius aperture at the expected stellar position in the MIPS 70 μm mosaics. The solid curve shows the expected S/N distribution for Gaussian noise (dispersion = 1.0) scaled to a peak value of N=67. The dashed curve shows a Gaussian with a dispersion of 1.49. These results suggest that the 70 μm photometric uncertainties are underestimated by a factor of 1.49. The uncertainties in the 70 μm flux densities reported in Table 1 have been scaled by this factor.

MIPS 70 μm photometry is calibrated to a theoretical PRF measured computed over a 64′ × 64′ field (Gordon et al. 2007). The aperture correction needed to place the background-subtracted flux densities measured in a finite aperture on the same scale as the theoretical PRF depends on the temperature of the underlying source emission. In anticipation that the FEPS MIPS 70 μm observations did not detect the stellar photosphere in most cases and that debris disks around solar-type stars have temperatures of $\sim$ 50–100 K, aperture corrections were measured on a 100 K PRF (Gordon et al. 2007). The aperture correction derived for our adopted aperture radius of 16″ and sky annulus between 40″ and 60″ is 1.766. By comparison, the SSC web pages indicate that the aperture of correction for a 3000 and 15 K PRF is 1.741 and 1.884, respectively, for the same 16″ aperture radius and similar, but not identical, background annulus of 39″–65″.

The MIPS 70 μm photometry and internal uncertainties are presented in Table 1. The FEPS sources where the 70 μm photometry was measured on PRF-subtracted images are marked in the table. The adopted calibration factor is 702.0 MJy sr^{-1}/(DN s^{-1}) with an uncertainty of 7% as reported on the SSC MIPS calibration web pages.[16]

5. IRS LOW-RESOLUTION SPECTRA

Low-resolution spectra ($\lambda/\delta\lambda \sim 60$–120) of the FEPS sources were obtained with IRS. Most sources were observed in the short-low 1 (SL1, 7.4–14.5 μm), long-low 2 (LL2, 14.0–21.3 μm), and long-low 1 (LL1, 19.5–38 μm) orders. A subset of sources were also observed in the short-low 2 (SL2, 5.2–7.7 μm) order. The spectral coverage beyond 35 μm suffers from low S/N and was discarded for all sources. The source HD 191089 was observed

[16] See http://ssc.spitzer.caltech.edu/mips/calib.

by a GTO program (PID 2; PI: J. Houck) and was not included in the FEPS IRS observations. Also, HD 72905 and HD 216803 were observed in the SL2 order only by FEPS; the longer wavelengths for HD 72905 were observed as part of a GTO program (PID 41; PI: G. Rieke).

Targets were acquired in the spectrograph slit using either high-accuracy IRS or PCRS peak-up with a 1 σ radial pointing uncertainty of 0.4″ and 0.14″, respectively, according to version 8.0 of the *Spitzer* Observing Manual. The reconstructed pointing from the peakup observations differed from the requesting pointing by >9″ for five sources: HD 80606, HD 139813, HII 2881, HIP 42491, and RX J1544.0−3311. We assumed that the spectra for these five sources are not for the intended target. For HD 13974, the pointing offset was within the pointing accuracy of the IRS peakup, but the intensity of the SL1 spectrum is a 2.6 times lower than expected by extrapolating the IRAC 8 μm photometry to 13 μm assuming a ν^2 spectrum. For R45, the extracted spectrum had a flux density less than 0 Jy for wavelengths >25 μm. We have excluded the SL and LL spectra for HD 13974 and R45, respectively.

Two nod positions per cycle were obtained for the IRS observations in standard staring mode with a minimum of six cycles per target to allow rejection of bad pixels and cosmic-ray hits. Each spectral image comes with a bit-mask image that marks potentially bad pixels. The data conditions identified by each bit in the mask are described in the *Spitzer* Data Handbook.[17] Pixels marked with bit 9 or higher were replaced with the average pixel value of an 8 pixel box surrounding the bad pixel. This method for finding the mean pixel value resembles Nagao-Matsuyama filtering (Nagao & Matsuyama 1979) and ensured edge preservation in the source region of our spectral images.

Source spectra were extracted from the droop intermediate data product from the SSC pipeline version S13 for all but two sources. The spectra for MML 18 and ScoPMS 52 were reobserved since the initial observations had a failed peakup, and the final spectra were extracted from S15 data products. Background emission and stray light were eliminated by subtracting images of the two slit positions at which a target is observed for each module and order. This resulted in a set of images containing a positive and negative spectrum in each observed order. A straight-sided (boxcar) aperture was used to extract the spectra for each nod position and cycle.

We found that the source positioning has the expected 0.4″ (1 σ) pointing accuracy, but that the targets are not positioned exactly on the $\frac{1}{3}-\frac{2}{3}$ position along the slit. The width of each aperture was determined by two quantities: the maximum size of the PSF in each order, and the pointing accuracy. The width of each aperture is chosen such that 99% of the source flux is within the aperture. To estimate the size of a point source we assume a Gaussian PSF with a FWHM $= 0.25^{*}\lambda$, where λ is in microns and FWHM is in arcseconds. Taking also the positioning constraints into account, the apertures are widened an additional 2.4″ (6 σ), to ensure that the entire source is always positioned within the aperture. The resulting extraction boxes were 6 pixels (11.1″) and 5 pixels (25.4″) along the slit for the short-low and long-low modules, respectively. Given that the slit width is only 2 pixels, pointing uncertainties in the dispersion direction will dominate the error on the flux density.

Because spectra were extracted with custom apertures that differ from the SSC processing, the spectral response function (SRF) had to be derived. We used a set of high S/N observations of bright calibration stars with model spectra provided by the SSC to derive the relative SRF, and then an internal calibration to determine the absolute flux calibration. Calibrating slit spectra suffers from uncertainties in the adopted spectral model and flux losses due to pointing offsets of the slit compared to the target. The FEPS Legacy program provides a unique opportunity to derive a good flux calibration for solar-type main-sequence stars since many stars do not exhibit emission from cool dust in the IRS wavelengths (Carpenter et al. 2008). The SRFs were determined for each order separately as the ratio of the observed spectrum to a Kurucz model spectrum using calibration stars identified in the FEPS program. The Kurucz model spectra were derived using the procedure outlined in Appendix C. Calibration stars were selected from the FEPS program by computing synthetic fluxes from the IRS spectra at wavelengths of 8, 13, 24, and 33 μm and applying the following criteria: (1) the flux density ratios of the synthetic photometry points at 8, 13, 24, and 33 μm are within 1 σ of the colors expected for stellar photospheres; (2) there were no known peak-up problems during data acquisition; (3) the spectra contains no artifacts from cosmic-ray hits, hot or dead pixels; and (4) the spectra have among the best S/N for the specific order and ramp time to ensure high-quality SRFs. The SRFs were derived from a set of 16 calibration stars for the SL1 and LL orders, and from a separate set of 10 stars for the SL2 order.

After the extraction of each spectrum and normalization by the SRF, a mean spectrum over all slit positions and cycles was computed for each individual order. The orders were then combined to form a single spectrum. In the regions where the spectra of the individual orders overlap, the flux densities were replaced by the mean flux density at each wavelength point. Internal uncertainties per pixel were estimated as the standard deviation of the mean of the repeated spectral observations. The SRF based on the bright calibration stars from the IRS instrument team (the spectra were extracted in an identical way to the FEPS sample) were then scaled to the SRF derived from the internal calibration described above. This procedure ensures that the uncertainties introduced by the adopted spectral model and flux losses due to pointing offsets of the slit are minimized and that the signal-to-noise ratio on the relative SRF is much better than that of the spectrum of any individual target.

The final calibrated spectra, excluding the problem spectra mentioned above, are distributed in the electronic version of this article. Each data file contains a header summarizing the observational parameters and four data columns that list the wavelength in microns, the flux density and internal uncertainty in Janskys, and the spectral order number.

6. SOURCE CONFUSION

Infrared cirrus and extragalactic sources may contaminate the FEPS photometry and create the appearance of an infrared excess. Since we anticipate that the emission associated with the stellar photosphere or a circumstellar disk will be nearly point-like and centered on the star at the typical distances in the FEPS sample, potential contamination to the 24 or 70 μm photometry can be identified from emission that is extended or offset from the stellar position.

We used the 2MASS catalog to represent the stellar position since most stars in the FEPS sample do not exhibit an infrared excess in the JHK_s bands (Carpenter et al. 2008), and any such excess should be unresolved spatially. 2MASS astrometry was corrected to the epoch of the *Spitzer* observations based on proper motions in the Tycho-2 (Høg et al. 2000) or UCAC2 (Zacharias et al. 2004) astrometric catalogs. MIPS 24 μm source coordinates were computed from the PRF centroid position and the WCS astrometric solution in the FITS image headers.

[17] See http://ssc.spitzer.caltech.edu/irs/dh.

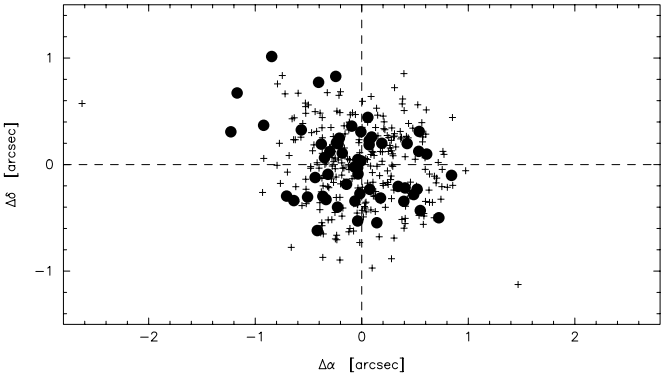

FIG. 4.—Angular offset between the 24 μm emission centroid and the 2MASS position after correcting for proper motion and differences in epoch of observations. Filled circles represent FEPS stars that exhibit an infrared excess in the IRS spectrum, and crosses represent sources without a detectable IRS excess (Carpenter et al. 2008).

In Figure 4 we show the angular separation between the 2MASS and MIPS 24 μm astrometry, where solid circles represent sources that exhibit an infrared excesses in the IRS spectra and crosses indicate stars without an excess (see Carpenter et al. 2008). Two sources have 24 μm positions that are offset by more than 1.8″ from the 2MASS coordinates, but neither exhibits an IRS infrared excess. Excluding these two outliers, the dispersion in the right ascension and declination offsets are 0.41″ and 0.36″, respectively, with a radial dispersion of 0.49″. The dispersion is dominated by uncertainties in the *Spitzer* astrometry since the typical 1 σ uncertainty in the 2MASS positions is ~0.14″ (Skrutskie et al. 2006). Stars with infrared excesses have a larger dispersion in the radial coordinate offsets than stars without infrared excesses (0.30″ vs. 0.23″), which can be attributed to three excess sources (HD 35850, HD 201219, and HD 209253) that have offsets of ~1.3″. The 24 μm excess source with the largest angular offset, which is HD 35850 at 1.35″, deviates from the 2MASS position by 2.9 σ in right ascension and 1.9 σ in declination. We conclude that for most FEPS sources, the 24 μm astrometry offsets relative to 2MASS is similar for stars with and without an infrared excess. Potentially three excesses sources may be contaminated by cirrus or extragalactic sources to produce an unusually large offset (1.3″). However, we cannot rule out pointing reconstruction errors since the two largest astrometric offsets are found around stars without infrared excesses.

The relative MIPS 70 μm and 2MASS astrometry was evaluated in a similar manner. We computed the 70 μm emission centroid by fitting a two-dimensional Gaussian to a 44″ × 44″ (11 × 11 mosaicked pixels) region centered on the expected stellar position. In Figure 5 we show the difference between the 70 μm and 2MASS astrometry as a function of the 70 μm S/N measured in a 16″ aperture. For sources with S/N ≥ 3, the positional agreement is better than 3.5″ for all but three sources: HD 201219 (5.1″ offset), HD 104467 (12.8″), and RX J1111.7−7620 (13.4″). RX J1111.7−7620 is separated by 24.4″ from the classical T Tauri star XX Cha; these sources have comparable brightness at 70 μm and the Gaussian fit converged to a centroid intermediate between the two sources. The 70 μm detection toward HD 104467 is a point source clearly offset from the stellar position. Given the large offset, we assume that the detected 70 μm source is unrelated to the star. Finally, the HD 201219 70 μm mosaic contains two point sources separated by 20.9″ that distorted the Gaussian fit. We fitted Gaussians to both sources and determined that the brighter of the two sources is 3.4″ from the 2MASS position for HD 201219, which is not unusual given the 70 μm S/N (5.9) for this source.

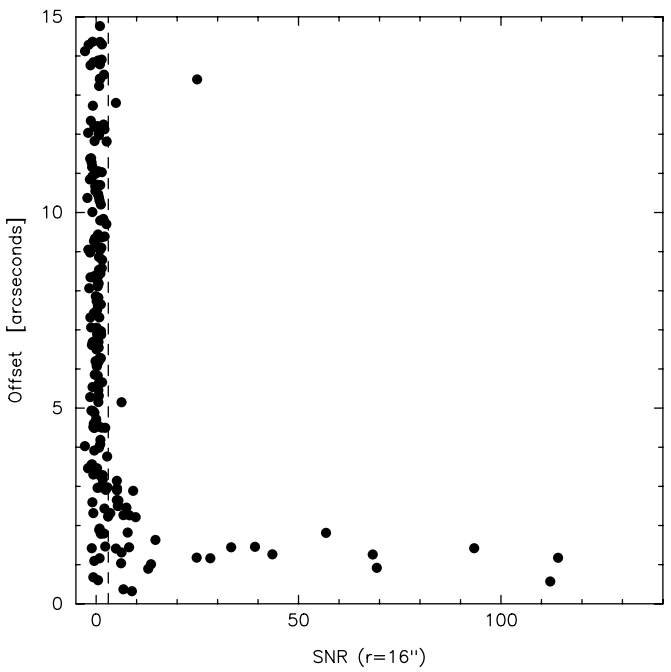

FIG. 5.—Angular offset between the 70 μm coordinates and the 2MASS stellar position as a function of the 70 μm S/N measured in a 16″ radius aperture. The 70 μm centroid was computed by fitting a two-dimensional Gaussian to a 44″ × 44″ region centered on the stellar position. The vertical dashed line at S/N = 3 indicates the minimum signal-to-noise ratio that defines a MIPS 70 μm detection. 2MASS coordinates have been corrected to the *Spitzer* epoch of observations using published proper motions.

However, this source also exhibits one of the larger angular offsets between the MIPS 24 μm astrometry and 2MASS. While neither the 24 μm nor the 70 μm astrometry conclusively demonstrates that the MIPS photometry for HD 201219 is contaminated, it suggests that the photometry for this source should be used with caution.

To further search for possible contaminants in the MIPS photometry, we computed the ratio of the flux measured in a large (10.2″ and 30″ for MIPS 24 and 70 μm, respectively) to a small (5.2″ and 16″ for MIPS 24 and 70 μm) aperture radius. A contaminating object or extended emission will create an anomalous ratio between aperture sizes. In Figure 6 we show the flux ratio measured in a large aperture to that in a small aperture as a function of the S/N for the MIPS 24 μm photometry. The scatter in the flux ratio is similar for sources with (*solid circles*) and without (*crosses*) 24 μm excesses. For S/N > 300, the source with the most discrepant flux ratio at 24 μm relative to the other sources is HD 107146 at S/N = 900. Several studies have demonstrated that this source is surrounded by a circumstellar disk (Ardila et al. 2004; Williams et al. 2004; Carpenter et al. 2005) and the observed flux ratio suggests that the source may be extended at 24 μm. Sources with a 24 μm S/N ratio less than 100 exhibit a larger scatter in flux ratios. The range of values is similar for sources with and without infrared excesses, and suggests that the scatter can be attributed to lower signal-to-noise in the larger photometric aperture.

In Figure 7 we show the flux ratio in the two aperture sizes as a function of the S/N for the MIPS 70 μm photometry. Two sources (HD 104467 and RX J1111.7−7620) with S/N > 3 have anomalously large ratios (>1.8). As discussed above, the initial photometry for these sources were contaminated by a nearby object, and the nearby source was PRF-subtracted before performing the final photometry. A third source (HD 216803) has a flux ratio

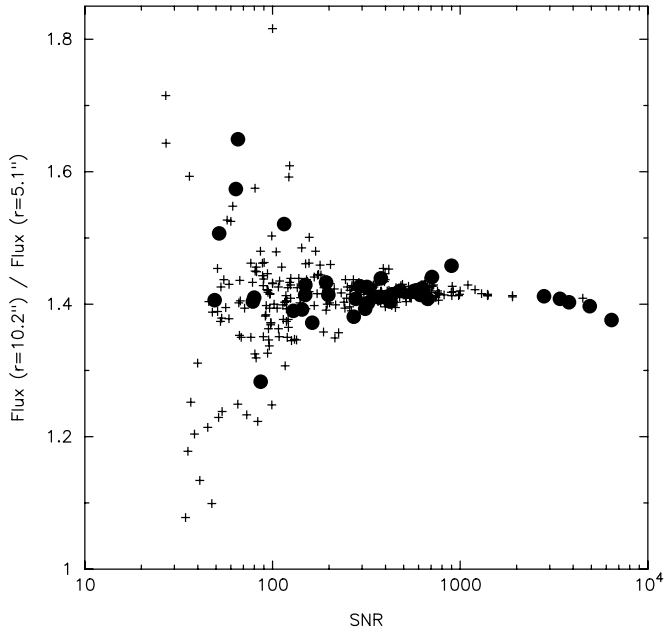

FIG. 6.—Ratio of the 24 μm flux density measured in a 10.2″ radius aperture (=4 pixels) to that in a 5.1″ radius aperture (=2 pixels) as a function of the S/N of the 24 μm PRF photometry. Filled circles represent sources with a $\geq 3\ \sigma$ 24 μm excess confirmed by the IRS spectrum, and crosses indicate sources without detectable 24 μm excesses (Carpenter et al. 2008).

just under 1.8. The 70 μm emission for this object is centered on the stellar position to within 3″, and the observed 70 μm emission is consistent with the expected stellar photosphere.

In summary, we conclude that the astrometry and curve-of-growth for most sources are consistent with point source emission centered on the stellar position. No compelling evidence exists

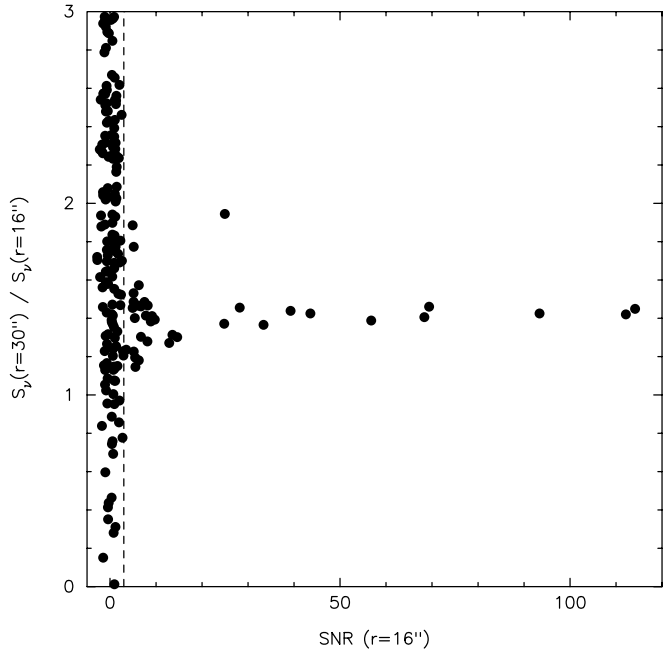

FIG. 7.—Ratio of the 70 μm flux density measured in a 30″ radius aperture to that in a 16″ radius aperture as a function of the signal to noise ratio. The vertical dashed line is drawn at S/N = 3. The two sources with S/N > 3 and flux density ratios greater than 1.8 have a nearby source that partially overlap the source aperture. These two contaminating sources were PRF-subtracted before performing the final photometry.

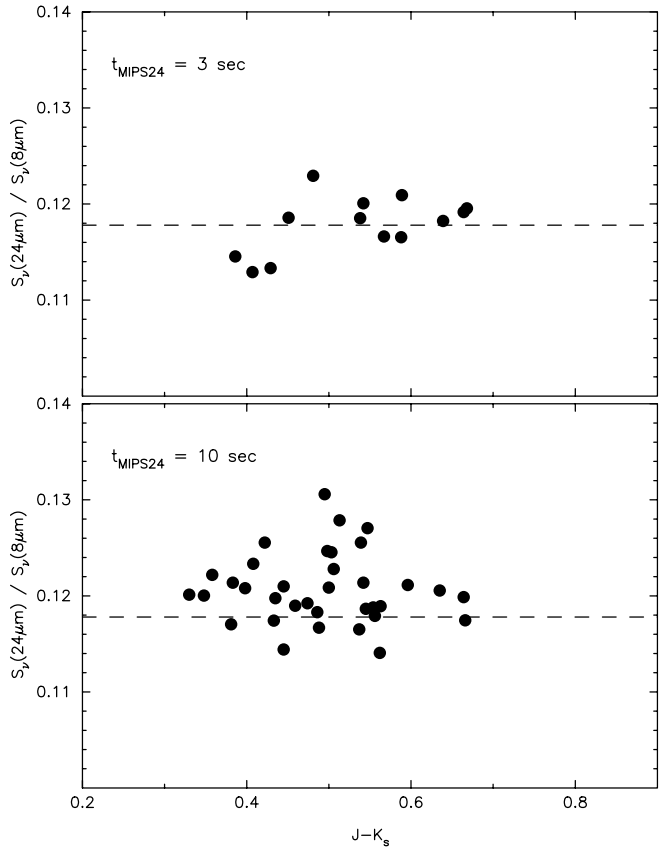

FIG. 8.—Ratio of 24 to 8 μm flux densities ($R_{24/8}$) plotted as a function of the $J - K_s$ color for stars observed with a 0.10 s IRAC frame time that do not have a IRS excess (see text for a complete description of the selection criteria). The top panel shows the results for stars observed with a MIPS 24 μm exposure time of 3 s, and the bottom panel for 10 s exposure time. The dashed line shows the mean flux ratios for the 3 s MIPS data. The ratio of the mean value of $R_{24/8}$ in the 3 s MIPS data to the 10 s data is 0.976 ± 0.008.

that contaminants systematically influence the 24 photometry. At 70 μm, contaminants needed to be removed for a few sources before measuring the final photometry, and the sources are noted in Table 1. These results do not exclude the possibility that the photometry for some sources may be contaminated, but any such contamination must be present in a minority of sources.

7. CROSS-INSTRUMENT CALIBRATION

In this section we use the FEPS data to examine the cross-instrument calibration. We first analyze the 24 to 8 μm flux density ratio, which plays a prominent role in a companion paper to identify sources that exhibit excess emission from circumstellar dust (Carpenter et al. 2008). We then compare the IRS and MIPS 24 μm calibration.

7.1. *IRAC 8 μm vs. MIPS 24 μm*

The observed IRAC 8 μm flux density is consistent with photospheric emission for most stars in the FEPS sample (Carpenter et al. 2008). The 24/8 μm flux ratio then is diagnostic of sources that exhibit circumstellar dust emission at 24 μm. The precision to which this ratio can identify excesses depends on the relative calibration stability of the IRAC and MIPS instruments over time and between the various observing modes.

The primary difference between observations of different stars is the exposure time for individual IRAC and MIPS images. We

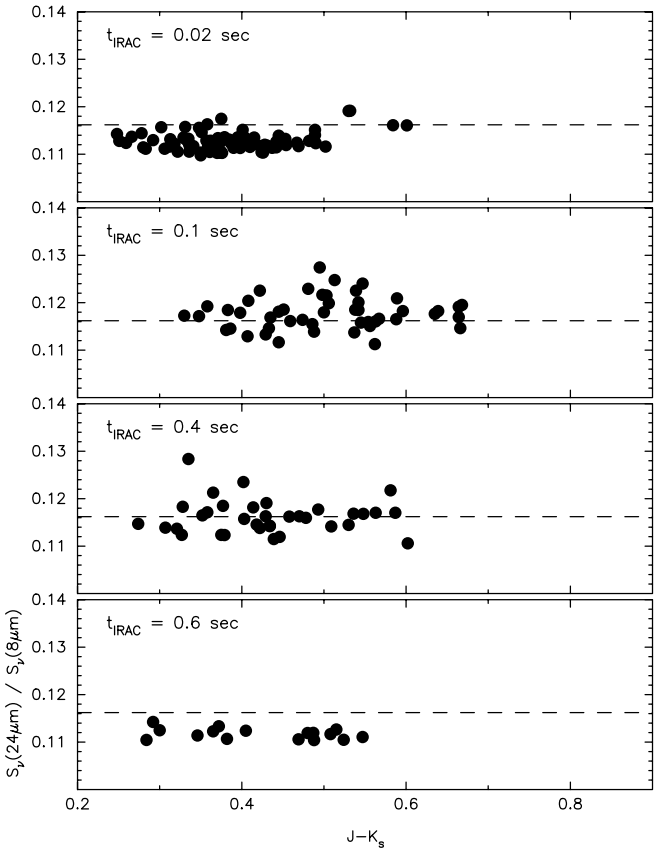

FIG. 9.—Ratio of 24 to 8 μm flux densities plotted vs. dereddened $J - K_s$ color for IRAC frame times of 0.02, 0.1, 0.4, and 0.6 s. The dashed line in each panel shows the mean flux ratio for the 0.4 s IRAC data. These results suggest that the observed 24/8 μm flux ratio varies with IRAC frame time.

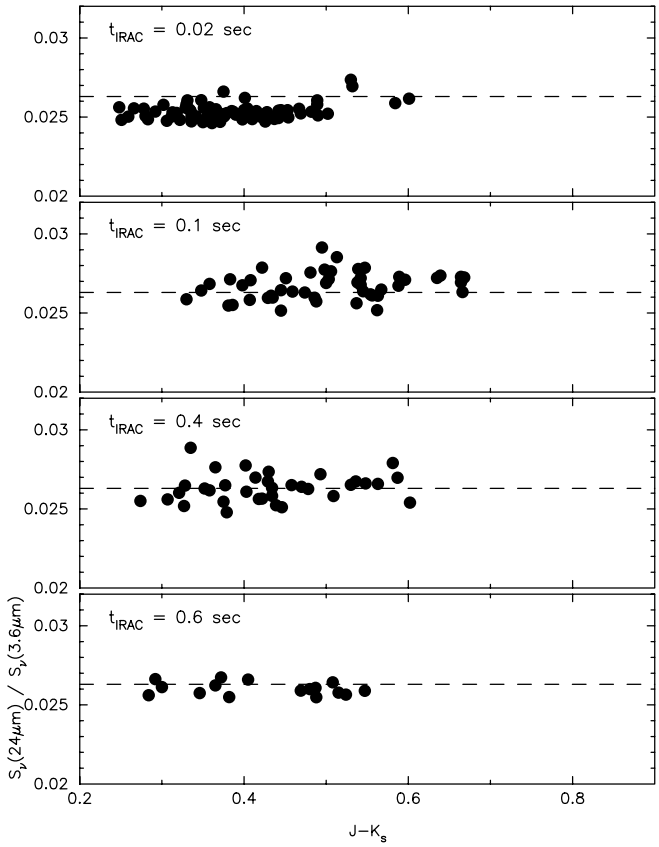

FIG. 10.—Same as Fig. 9, but for the IRAC 3.6 μm band.

first examine the relative stability of the MIPS 24 μm calibration by selecting stars in the FEPS program that were observed with the same IRAC frame time, but different MIPS exposure times. We selected 48 stars in the FEPS sample that (1) have been observed with IRAC frame times of 0.10 s, (2) do not show evidence for more than a 2 σ infrared excesses in the FEPS IRS spectra (Carpenter et al. 2008) to ensure the 24 μm emission is from the photosphere, (3) the variation in the encircled energy with aperture radius in the IRAC images is consistent with a point source (see § 2.2), and (4) the dereddened $J - K_s$ color is less than 0.7 mag to remove the intrinsically reddest stars in the FEPS sample. We used a 0.10 s IRAC frame time to obtain the largest sample of stars observed with different MIPS exposure times.

In Figure 8 we plot the 24/8 μm flux density ratio ($\equiv R_{24/8}$) for MIPS 3 s (*top panel*) and 10 s (*bottom panel*) exposure times versus the dereddened 2MASS $J - K_s$ color using the extinction estimates derived in § B.1. The two sample of stars span similar ranges of dereddened $J - K_s$ colors, and we assume that the two samples also share the same intrinsic photospheric $[8] - [24]$ color. The Shapiro-Wilk statistic ($\equiv p_{\rm SW}$) indicates that the distribution of observed data points about the mean is consistent with a normal distribution for each sample ($p_{\rm SW} = 0.76$ for the 3 s MIPS data and $p_{\rm SW} = 0.31$ for the 10 s data). The Student's *t*-test then can be used to compare the mean values of $R_{24/8}$ for the 3 and 10 s MIPS data. The probability from the *t*-test that the mean values of $R_{24/8}$ for the two samples are consistent with each other is 0.009. The ratio of the mean value of $R_{24/8}$ in a 3 s MIPS exposure to that in a 10 s exposure is 0.976 ± 0.008, where the uncertainty was computed as the standard deviation of the mean. These results suggest that the mean $R_{24/8}$ value is higher for the 10 s MIPS data on average compared to the 3 s data.

Engelbracht et al. (2007) measured directly any MIPS 24 μm calibration offsets by observing a sample of 11 stars with 3, 10, and 30 s MIPS exposure times. They also found that the measured flux densities were larger on average in 10 s exposure data compared to 3 s observations. However, the magnitude of their offset (1%) is 2.4 times smaller than the offset derived from the FEPS data. While the reduction procedure adopted here attempted to follow that recommended by Engelbracht et al. (2007) our data processing was nonetheless performed using SSC products and custom software that could account for the different results. Also, we adopted PRF-fitting photometry, while Engelbracht et al. (2007) used aperture photometry. As a check of our data reduction methods, we compared our photometry with the results from Rieke et al. (2008), who used the pipeline described in Engelbracht et al. (2007) to process data for 31 FEPS sources that were observed with 3 s exposure times. For these 31 stars, the median difference between the flux densities measured by FEPS and Rieke et al. (2008) is 0.0% with a dispersion of 2.6%. Therefore our data reduction procedures for at least the 3 s exposure data yields photometry consistent with the Engelbracht et al. (2007) processing, but no independent check is available for the 10 s MIPS data.

We now consider the relative flux calibration for stars with different IRAC exposure times. In Figure 9 we plot the 24/8 μm flux density ratio versus dereddened $J - K_s$ color for stars observed with various IRAC frame times. The MIPS 24 μm photometry obtained with 10 s exposure times have been scaled by a factor of 0.976 based on the analysis above since the MIPS calibration is tied mainly to data obtained with 3 s exposure times

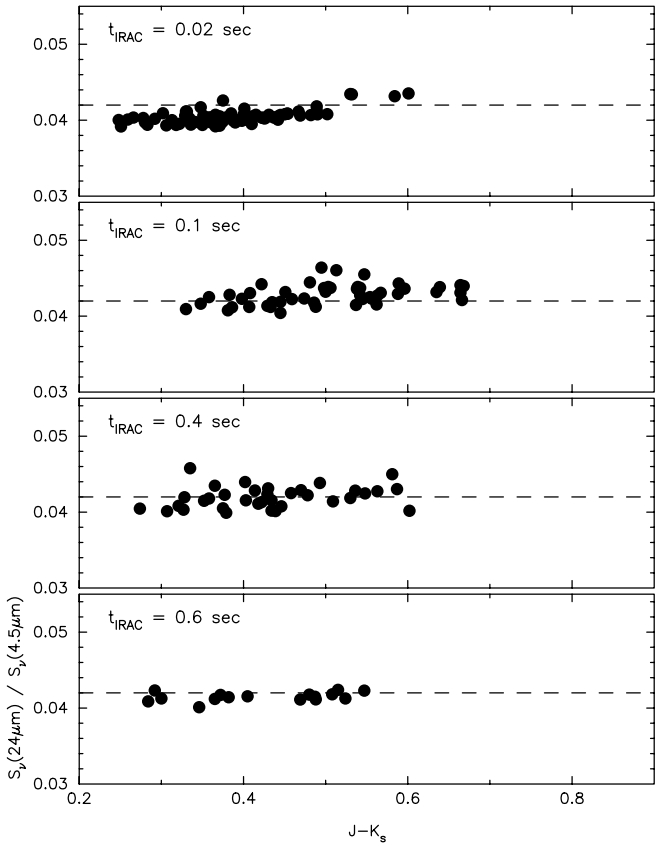

FIG. 11.—Same as Fig. 9, but for the IRAC 4.5 μm band.

(Engelbracht et al. 2007). As shown in the figure, systematic differences are present in the mean flux density ratio between the various IRAC frame times. Offsets are present even if the 10 s MIPS 24 μm data are not scaled, but the magnitude of the offset changes. We adopt the 0.4 s frame time as the fiducial calibration since the calibration of the 0.4 s subarray data and the full-array data are the same to within 1% (see § 2.2). A multiplicative scale factor of 0.971 ± 0.005 must be applied to the 0.02 s IRAC frame-time data to force agreement with the 0.4 s data, 1.014 ± 0.007 for the 0.1 s data, and 0.962 ± 0.006 for the 0.6 s data, where the uncertainties are the standard deviation of the mean. In Figures 10 and 11 we present a similar analysis for the IRAC 3.6 and 4.5 μm bands which demonstrates that offsets are also present in these bands. Since only five FEPS stars were observed in the IRAC 5.8 μm band, we were unable to derive offsets for that band.

Table 2 summarizes the multiplicative factors that must be applied to the flux ratios as a function of frame time to scale the calibration to the 0.4 s frame time data. The offsets are similar in the three bands for a given frame time, although the offset in the 0.6 s frame-time data may be larger for IRAC 8 μm than in the 3.6 and

TABLE 2
IRAC CALIBRATION OFFSETS RELATIVE TO 0.40 s FRAME TIME

BAND (μm)	IRAC FRAME TIME		
	0.02 s	0.10 s	0.60 s
3.6.....	0.961 ± 0.006	1.014 ± 0.007	0.988 ± 0.007
4.5.....	0.964 ± 0.006	1.021 ± 0.007	0.988 ± 0.007
8.0.....	0.971 ± 0.005	1.014 ± 0.007	0.962 ± 0.006

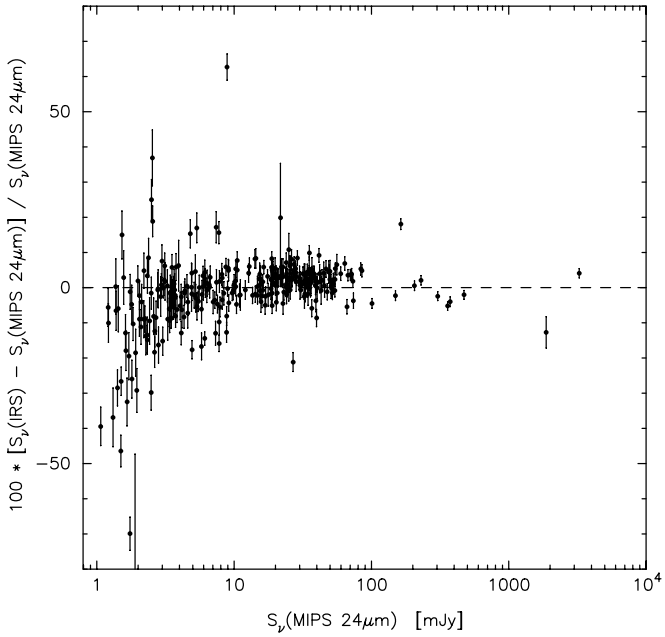

FIG. 12.—Percent difference between the synthetic IRS 24 μm photometry and MIPS 24 μm photometry as a function of the MIPS 24 μm flux density. The IRS 24 μm photometry was computed by integrating the observed IRS spectrum over the MIPS 24 μm bandpass. The horizontal dashed line is shown for reference.

4.5 μm bands. We consider these correction factors preliminary since they have not yet been verified by observing the same star with different frame times. No corrections for any integration-dependent calibrations have been applied to the photometry in Table 1, but the frame times are listed to enable the corrections to be applied by the reader.

7.2. *IRS vs. MIPS 24 μm*

The IRS spectral coverage encompasses the spectral response of the MIPS 24 μm bandpass. To compare the relative calibration of the two instruments, we computed synthetic 24 μm photometry from the IRS spectrum and the MIPS 24 μm spectral response using the procedure described in Appendix C2.

In Figure 12 we plot the percent difference between the IRS synthetic photometry and MIPS 24 μm photometry as a function of the MIPS 24 μm flux density. No exposure-time-dependent corrections have been applied to the MIPS 24 μm flux densities for this analysis. For sources brighter than 10 mJy, which have the highest S/N, the median difference in the 24 μm flux densities between the IRS spectra and the MIPS photometry is 2.1%. The median difference for sources between 3 and 10 mJy is -1.6%. These differences are within the 1σ calibration uncertainty for both MIPS (4%; Engelbracht et al. 2007) and IRS (>5%; Infrared Spectrograph Data Handbook ver. 3.1). However, for individual sources, the difference between the MIPS and IRS flux densities are larger than expected based on the quantifiable internal uncertainties. One significant discrepancy is ScoPMS 52, where the IRS 24 μm flux density is 63% higher than the MIPS 24 μm flux density. Inspection of the MIPS 24 μm image shows that there is a source 18″ away that is an order of magnitude brighter than ScoPMS 52 (see Bouwman et al. 2008), and this source likely contributes flux to the IRS spectrum.

8. SUMMARY

The FEPS *Spitzer* Legacy program was designed to obtain infrared photometry from 3.6 to 160 μm and low-resolution spectra

from 5 to 35 μm for 328 solar-type stars spanning ages from 3 Myr to 3 Gyr. The broad goal of FEPS was to determine the incidence of circumstellar disks and place the results in context with the expected evolution of our solar system. An essential component of this study was to construct carefully calibrated SEDs. Here, we outline the data reduction procedures adopted by the FEPS team to obtain accurate and well-characterized *Spitzer* photometry and spectra.

The adopted image processing steps for the IRAC, MIPS, and IRS data closely follow the recommended procedures by the *Spitzer* Science Center and *Spitzer* Instrument Teams. We describe in detail the data reduction methods for each instrument and the procedures used to validate the data products. We present in Table 1 the measured IRAC (3.6, 4.5, and 8 μm bands) and MIPS (24 and 70 μm) flux densities and uncertainties. The extracted, calibrated IRS spectra are available electronically.

J. M. C. thanks Dave Frayer, Sean Carey, Bill Reach, Jason Surace, and the staff at the *Spitzer* Science Center for patiently answering numerous questions regarding *Spitzer* data. We are grateful to the anonymous referee and George Rieke for providing valuable comments. We also thank Debbie Padgett, Tim Brooke, Dan Watson, Pat Morris, and the rest of the FEPS team for their many contributions throughout this project. This work is based on observations made with the *Spitzer Space Telescope*, which is operated by JPL/Caltech under a contract with NASA. The program made use of data and resources from the FEPS project, which receives support from NASA contracts 1224768, 1224634, and 1224566 administered through JPL. This research made use of the SIMBAD database, operated at CDS, Strasbourg, France, as well as data products from the Two Micron All Sky Survey, which is a joint project of the University of Massachusetts and the Infrared Processing and Analysis Center/Caltech, funded by NASA and the NSF.

APPENDIX A

STELLAR PHOTOMETRY

The FEPS team obtained optical photometry in the *BVRI* broadband filters for 45 stars. Observations were obtained with the 61″ Kuiper Telescope on 2003 May 8 and 2003 September 29–30, and the CTIO 0.9 m telescope on 2004 March 18–21.

The Kuiper observations used a 2048×2048 pixel CCD with a pixel scale of 0.45″ pixel^{-1}. Images were processed by subtracting the bias, dividing by a "master" flat field created from sky observations to remove large-scale response variations over the CCD, and dividing by a dome flat to remove pixel-to-pixel variations. The CTIO observations were performed with a 2048×2048 CCD and a pixel scale of 0.40″ pixel^{-1}. The CCD is read out with different amplifiers for each quadrant. Each quadrant was bias subtracted and divided by dome flats.

Photometry was measured using aperture photometry with a sky annulus that extended from 20 to 30 pixels, and an aperture radius of 11 and 12 pixels for the CTIO and Kuiper images, respectively. Eight FEPS stars had a nearby source in projection, and a smaller aperture radius between 2–3 pixels to isolate the photometry to the FEPS target. The observations were calibrated by observing multiple standard stars from Landolt (1992) to solve for the air mass coefficient, the photometric zero point, and color terms to place the photometry on the Johnson-Cousins photometric system. Total photometric uncertainties were computed as the rms sum of internal photometric uncertainties, the zero point, and the color terms. The photometry for the 45 sources are presented in Table 3.

APPENDIX B

STELLAR PROPERTIES

In this section we describe the procedure to assign estimates of the visual extinction, surface gravity, metallicity, and effective temperature for each star in the FEPS sample. These derived parameters were used in several FEPS studies, and served as initial estimates for the Kurucz model fitting (see Appendix C).

B1. VISUAL EXTINCTION

Distances to the FEPS targets extend upwards of 343 pc and the extinction from the interstellar medium may be nonnegligible. The visual extinction toward individual stars was estimated from one of the following techniques in priority order: (1) proximity within the Local Bubble, (2) as a member of stellar cluster that has been extensively studied previously; (3) color excess at optical and near-infrared wavelengths; and (4) a galactic extinction model. We now describe each of these techniques.

Stars within the Local Bubble are expected to have small extinction at visual wavelengths. The size of the Local Bubble has been measured by observing interstellar absorption lines toward stars with known distances, and then determining the column density as a function of distance. Welsh et al. (1998) present an analysis of Na I column density measurements toward stars with *Hipparcos* distance estimates, and they found that the visual extinction is less than 0.01 mag out to a distance of $d = 75$ pc. We adopted an extinction of 0 mag for the 169 stars in the FEPS sample where $d + 3\Delta d \leq 75$ pc, where Δd is the 1 σ distance uncertainty (see Meyer et al. 2006 for a discussion on the distance determinations).

The visual extinction toward the clusters in the FEPS sample has been extensively studied in the literature. For the Hyades, Taylor (2006) place an upper limit at 95% confidence of $E(B - V) = 0.001$ mag, and we adopt $A_V = 0$ mag. Breger (1986) compiled spectral types and optical photometry for about 120 Pleiades members and derived $E(B - V) = 0.04$ on average, but with lower reddening to the east of the cluster (0.03 mag) compared to the west (0.06 mag). Assuming a factor of 3.1 to convert the $B - V$ reddening to visual extinction, we adopt a constant value of 0.12 mag for the Pleiades stars. Following Pinsonneault et al. (1998), we adopt an average $E(B - V) = 0.10$ (see Crawford & Barnes 1974; Prosser 1992), or $A_V = 0.31$ mag, for Alpha Per. For IC 2602, we adopt a visual extinction of 0.12 mag (Whiteoak 1961).

Many of the FEPS stars are field objects that have distances greater than 75 pc. The visual extinction for these stars was computed from the color excess given the published spectral types (see Meyer et al. 2006) and observed colors. Optical (Johnson B and V, Tycho B_T and V_T)

TABLE 3
NEW *BVRI* PHOTOMETRY FOR FEPS SOURCES

Source	B_J	V_J	R_C	I_C
1E 0307.4+1424	11.129 ± 0.030	10.463 ± 0.025	10.045 ± 0.023	9.693 ± 0.023
1E 0324.1−2012	11.049 ± 0.037	10.435 ± 0.031	10.082 ± 0.028	9.726 ± 0.024
1RXS J025216.9+361658	11.839 ± 0.031	10.715 ± 0.026	10.016 ± 0.019	9.369 ± 0.024
1RXS J025751.8+115759	11.645 ± 0.031	10.797 ± 0.026	10.266 ± 0.024	9.799 ± 0.024
1RXS J031644.0+192259	11.598 ± 0.030	10.996 ± 0.025	10.598 ± 0.023	10.248 ± 0.023
1RXS J031907.4+393418	12.444 ± 0.030	11.653 ± 0.025	11.159 ± 0.023	10.734 ± 0.023
1RXS J035028.0+163121	11.257 ± 0.030	10.567 ± 0.025	10.096 ± 0.023	9.701 ± 0.023
1RXS J051111.1+281353	11.492 ± 0.053	10.522 ± 0.028	9.933 ± 0.030	9.398 ± 0.028
1RXS J053650.0+133756	11.482 ± 0.054	10.551 ± 0.028	9.994 ± 0.032	9.496 ± 0.028
2RE J0255+474	11.773 ± 0.033	10.723 ± 0.027	10.052 ± 0.027	9.497 ± 0.026
BPM 87617	12.013 ± 0.037	10.849 ± 0.025	10.154 ± 0.016	9.486 ± 0.016
HD 279788	11.452 ± 0.030	10.640 ± 0.025	10.137 ± 0.023	9.704 ± 0.023
HD 286264	12.050 ± 0.055	10.889 ± 0.023	10.144 ± 0.033	9.451 ± 0.028
MML 18	11.790 ± 0.004	10.803 ± 0.004	10.231 ± 0.004	9.697 ± 0.004
MML 28	12.385 ± 0.005	11.347 ± 0.006	10.753 ± 0.004	10.203 ± 0.005
MML 38	11.786 ± 0.003	10.957 ± 0.004	10.454 ± 0.003	9.954 ± 0.004
MML 40	11.527 ± 0.003	10.665 ± 0.005	10.161 ± 0.003	9.679 ± 0.005
MML 51	12.203 ± 0.005	11.131 ± 0.005	10.492 ± 0.005	9.884 ± 0.005
[PZ99] J155847.8−175800	13.164 ± 0.046	11.875 ± 0.031	11.152 ± 0.020	10.403 ± 0.019
[PZ99] J160814.7−190833	12.593 ± 0.066	11.458 ± 0.032	10.829 ± 0.021	10.241 ± 0.021
[PZ99] J161318.6−221248	11.493 ± 0.045	10.397 ± 0.030	9.783 ± 0.020	9.165 ± 0.019
[PZ99] J161329.3−231106	12.836 ± 0.045	11.693 ± 0.031	11.033 ± 0.020	10.339 ± 0.020
[PZ99] J161402.1−230101	12.379 ± 0.046	11.353 ± 0.031	10.777 ± 0.020	10.197 ± 0.020
[PZ99] J161411.0−230536	11.824 ± 0.046	10.671 ± 0.032	10.025 ± 0.021	9.377 ± 0.020
[PZ99] J161459.2−275023	12.133 ± 0.048	11.194 ± 0.033	10.666 ± 0.021	10.153 ± 0.021
[PZ99] J161618.0−233947	11.603 ± 0.047	10.659 ± 0.032	10.126 ± 0.021	9.593 ± 0.021
RX J0258.4+2947	...	11.378 ± 0.039	10.853 ± 0.033	10.361 ± 0.033
RX J0331.1+0713	11.610 ± 0.031	10.719 ± 0.026	10.145 ± 0.024	9.608 ± 0.024
RX J0357.3+1258	11.691 ± 0.031	10.994 ± 0.026	10.547 ± 0.023	10.132 ± 0.024
RX J0434.3+0226	13.557 ± 0.028	12.554 ± 0.020	11.897 ± 0.016	11.253 ± 0.019
RX J0442.5+0906	11.974 ± 0.056	11.186 ± 0.029	10.720 ± 0.033	10.301 ± 0.029
RX J1450.4−3507	11.578 ± 0.004	10.651 ± 0.003	10.091 ± 0.002	9.538 ± 0.003
RX J1457.3−3613	10.966 ± 0.004	10.201 ± 0.003	9.748 ± 0.002	9.332 ± 0.003
RX J1458.6−3541	11.762 ± 0.005	10.724 ± 0.003	10.089 ± 0.002	9.476 ± 0.003
RX J1500.8−4331	11.960 ± 0.012	11.099 ± 0.004	10.584 ± 0.004	10.074 ± 0.006
RX J1518.4−3738	11.688 ± 0.012	10.826 ± 0.004	10.313 ± 0.004	9.817 ± 0.006
RX J1531.3−3329	11.687 ± 0.012	10.874 ± 0.004	10.391 ± 0.004	9.937 ± 0.006
RX J1541.1−2656	12.099 ± 0.013	11.210 ± 0.005	10.658 ± 0.006	10.168 ± 0.007
RX J1544.0−3311	11.868 ± 0.009	10.953 ± 0.005	10.411 ± 0.004	9.858 ± 0.007
RX J1600.6−2159	12.140 ± 0.045	11.088 ± 0.030	10.518 ± 0.019	9.962 ± 0.019
RX J1839.0−3726	12.035 ± 0.010	11.092 ± 0.006	10.529 ± 0.005	9.996 ± 0.009
RX J1842.9−3532	12.895 ± 0.010	11.998 ± 0.006	11.313 ± 0.004	10.653 ± 0.008
RX J1844.3−3541	12.213 ± 0.008	11.184 ± 0.005	10.555 ± 0.004	9.940 ± 0.007
RX J1852.3−3700	13.343 ± 0.008	12.219 ± 0.005	11.510 ± 0.004	10.810 ± 0.007
W79	12.304 ± 0.004	11.499 ± 0.004	11.043 ± 0.004	10.638 ± 0.004

and near-infrared (2MASS J, H, and K_s) photometry were compiled from the literature (see Appendix C1) or measured by the FEPS team (see Appendix A). The intrinsic colors as a function of spectral type were compiled from the literature by cross-correlating the *Hipparcos* catalog with the Michigan Spectral Catalog, Tycho-2, and 2MASS. The positional match between the Tycho-2 and Michigan spectral atlas from Wright et al. (2003) was used as a starting point. Only 2MASS sources with a PH_QUAL flag of AAA and a confusion flag of 000 were used. A photometric uncertainty of less $\leq$0.072 mag (i.e., signal-to-noise ratio >15) was required in each photometric band. The average color was then computed as a function of spectral type for stars within 75 pc for B and V photometry, and within 100 pc for colors involving J, H, and K_s. In computing the average colors, individual measurements were weighted by the inverse variance of the measurements, and outliers from poor photometry or spectral types were removed in an iterative sigma-clipping procedure. Table 4 lists the adopted intrinsic colors for the relevant spectral types in the FEPS sample, the dispersion in the observed colors, and the number of stars that met the above criteria. Color excesses were computed from the observed $(B-V)_{\rm Johnson}$, $(B-V)_{\rm Tycho}$, $V_{\rm Tycho}-K_s$, and $J-K_s$ colors and the intrinsic colors listed in Table 4. Intrinsic $(B-V)_{\rm Johnson}$ colors were computed from the $(B-V)_{\rm Tycho}$ colors and the Tycho-to-Johnson transformation equations in Mamajek et al. (2002, 2006). The visual extinction was estimated for each color using the extinction law compiled by Mathis (1990) and the weighted mean was adopted as the extinction.

For nine stars, the visual extinction could not be estimated with the above techniques since either a spectral type was not available, or the computed extinction was unphysical (i.e., $A_V < 0$ mag). In the latter case, it is presumed that the photometry was poor or the spectral type is erroneous. For these stars, we estimated the extinction using the Sandage (1972) extinction model assuming an exponential disk (see

TABLE 4
ADOPTED INTRINSIC COLORS

	$(B-V)_T$			$J-K_s$			V_T-K_s		
SPECTRAL TYPE	Average	Dispersion	N	Average	Dispersion	N	Average	Dispersion	N
F2	0.383	0.028	74	0.224	0.029	153	0.980	0.093	58
F3	0.433	0.025	147	0.237	0.019	257	1.090	0.057	102
F5	0.483	0.022	266	0.267	0.026	491	1.216	0.069	230
F6	0.527	0.022	214	0.288	0.020	337	1.305	0.058	173
F7	0.558	0.026	250	0.303	0.025	371	1.354	0.050	177
F8	0.592	0.023	130	0.320	0.025	211	1.393	0.043	90
G0	0.632	0.025	206	0.329	0.021	313	1.460	0.041	145
G1	0.648	0.023	114	0.342	0.025	197	1.498	0.067	117
G2	0.669	0.025	167	0.350	0.024	248	1.554	0.069	166
G3	0.707	0.033	324	0.371	0.029	521	1.601	0.047	241
G5	0.754	0.029	331	0.387	0.026	503	1.682	0.064	325
G6	0.801	0.036	175	0.417	0.025	211	1.759	0.059	144
G8	0.852	0.039	186	0.445	0.035	246	1.866	0.088	191
K0	0.936	0.040	183	0.490	0.043	224	2.032	0.124	196
K1	1.001	0.036	102	0.528	0.034	117	2.176	0.095	100
K2	1.064	0.051	95	0.574	0.035	96	2.334	0.114	91
K3	1.150	0.073	98	0.605	0.041	91	2.483	0.126	83
K4	1.272	0.061	43	0.703	0.054	51	2.800	0.160	42
K5	1.420	0.093	22	0.781	0.043	21	3.237	0.222	21

Chen et al. 1998). Finally, the FEPS sources studied by Bouwman et al. (2008) may have excess emission at K band from a circumstellar disk. For these sources, we estimated the extinction using the observed $(R-I)_C$ colors, the intrinsic colors compiled by Kenyon & Hartmann (1995) and the reddening law from Taylor (1986). The adopted extinction values are listed in Table 5.

B2. STELLAR EFFECTIVE TEMPERATURE, SURFACE GRAVITY, AND METALLICITY

The stellar effective temperature, surface gravity, and metallicity are needed to fit the Kurucz model atmospheres (see Appendix C). This section summarizes the procedure to estimate these properties for the FEPS sample. The procedure depends on the stellar age, as solar-mass stars younger than ~ 100 Myr are contracting toward the main sequence and the surface gravity varies with age.

Stars older than 100 Myr in the FEPS sample were considered to be main-sequence stars and were assigned a surface gravity of $\log g = 4.50$. Stellar effective temperatures were estimated from the $B-V$ and $V-K$ versus temperature relations derived by Houdashelt et al. (2000) after dereddening the observed photometry (see § B.1). If the temperature uncertainty derived from the photometry is larger than 130 K, the temperature was instead computed from a temperature versus spectral type relation using the colors listed in Table 4, the Tycho-to-Johnson color transformations from Mamajek et al. (2002, 2006) and the Houdashelt et al. (2000) color-temperature relations. A limit of 130 K was adopted since that is approximately the temperature uncertainty associated with ± 2 spectral subclasses.

Solar-type stars younger than 100 Myr will be contracting toward the main sequence and will generally have lower surface gravities. Derivation of the surface gravities and effective temperatures need to be solved jointly. First, the effective temperature was computed assuming the star is on the main sequence as described above. The surface gravity was then estimated from the D'Antona & Mazzitelli (1997) pre–main-sequence evolutionary tracks using the derived temperature and assumed age from Hillenbrand et al. (in preparation). If the temperature was estimated from the spectral type, an iterative correction needs to be applied since the derived temperature depends on both the spectral type and surface gravity. For the estimated surface gravity, a new temperature was derived using the effective temperature as a function of spectral type and surface gravity relation in Gray (1992). With the new temperature, the surface gravity was rederived from the D'Antona & Mazzitelli (1997) evolutionary tracks.

Finally, the metallicity was fixed to $[\mathrm{Fe/H}] = 0.13$ for the Hyades stars following the measurements from Paulson et al.2003). For all other stars, we assumed $[\mathrm{Fe/H}] = 0$. The adopted metallicity, effective temperature, and surface gravity for each star in the FEPS sample are listed in Table 5.

APPENDIX C

MODEL PHOTOSPHERES

In several FEPS studies, the observed *Spitzer* flux densities were compared to model photospheric flux densities to infer the presence of an infrared excess diagnostic of a circumstellar disk. Model flux densities were estimated from synthetic photosphere spectra computed by R. Kurucz[18] from ATLAS 9 stellar atmospheric models with convective overshoot and a microturbulent velocity of 1 km s^{-1}. In this section we describe the procedures used to normalize the synthetic spectra to observed photometry and to compute model flux densities.

[18] See http://kurucz.harvard.edu.

TABLE 5
ADOPTED STELLAR PROPERTIES

Source	Spectral Type	A_V (mag)	[Fe/H] (dex)	$\log g$ ($\log$ cm s^{-2})	$T_{\rm eff}$ (K)
1E 0307.4+1424	G6 V	0.03	0.00	4.54	5591
1E 0324.1−2012	G4 V	0.04	0.00	4.54	5745
1RXS J025216.9+361658	K2 IV	0.95	0.00	4.63	4999
1RXS J025751.8+115759	G7 V	0.62	0.00	4.54	5552
1RXS J030759.1+302032	G5 IV	0.16	0.00	4.50	5676
1RXS J031644.0+192259	G2 V	0.10	0.00	4.47	5886
1RXS J031907.4+393418	K0 V	0.19	0.00	4.61	5287
1RXS J034423.3+281224	G7 V	0.05	0.00	4.54	5725
1RXS J035028.0+163121	G5 IV	0.34	0.00	4.54	5725
1RXS J043243.2−152003	G4 V	0.37	0.00	3.89	5760
1RXS J051111.1+281353	K0 V	0.86	0.00	4.08	5325
1RXS J053650.0+133756	K0 V	0.56	0.00	4.50	5323
2RE J0255+474	K5 Ve	0.00	0.00	4.71	4714
AO Men	K3.5 V ke	0.00	0.00	4.41	4435
AP 93	...	0.31	0.00	4.68	4914
B102	...	0.12	0.00	4.54	5708
BPM 87617	K5 Ve	0.00	0.00	4.71	4419
HD 105	G0 V	0.00	0.00	4.48	5960
HD 377	G2 V	0.00	0.00	4.47	5851
HD 691	K0 V	0.00	0.00	4.50	5441
HD 984	F7 V	0.00	0.00	4.40	6227
HD 6434	G2/3 V	0.00	0.00	4.50	5804
HD 6963	G7 V	0.00	0.00	4.50	5518
HD 7661	K0 V	0.00	0.00	4.50	5399
HD 8907	F8	0.00	0.00	4.50	6250
HD 8941	F8 IV−V	0.00	0.00	4.50	6234
HD 9472	G0	0.00	0.00	4.50	5686
HD 11850	G5	0.00	0.00	4.50	5597
HD 12039	G3/5 V	0.00	0.00	4.54	5688
HD 13382	G5 V	0.00	0.00	4.50	5751
HD 13507	G5 V	0.00	0.00	4.50	5627
HD 13531	G7 V	0.00	0.00	4.50	5563
HD 13974	G0 V	0.00	0.00	4.50	5858
HD 15526	G5/6 V	0.13	0.00	4.54	5658
HD 17925	K1 V	0.00	0.00	4.68	5116
HD 18940	G0	0.00	0.00	4.50	5760
HD 19019	F8	0.00	0.00	4.50	6051
HD 19668	G8/K0 V	0.00	0.00	4.50	5414
HD 21411	G8 V	0.00	0.00	4.50	5500
HD 22179	G0	0.13	0.00	4.21	6000
HD 25300	K0	0.00	0.00	4.50	4329
HD 25457	F7 V	0.00	0.00	4.50	6173
HD 26182	G0 V	0.34	0.00	4.47	6026
HD 26990	G0(V)	0.00	0.00	4.50	5651
HD 27466	G5 V	0.00	0.00	4.50	5757
HD 28495	G0	0.00	0.00	4.50	5217
HD 29231	G8 V	0.00	0.00	4.50	5421
HD 31143	K0 V	0.00	0.00	4.50	5313
HD 31281	G1(V)	0.14	0.00	4.03	5927
HD 31392	K0 V	0.00	0.00	4.50	5360
HD 31950	...	0.13	0.00	4.40	6108
HD 32850	G9 V	0.00	0.00	4.50	5208
HD 35850	F7/8 V	0.00	0.00	4.04	6021
HD 37006	G0	0.00	0.00	4.50	5503
HD 37216	G5	0.00	0.00	4.50	5387
HD 37484	F3 V	0.00	0.00	4.27	6664
HD 37572	K0 V	0.00	0.00	4.67	5091
HD 37962	G5 V	0.00	0.00	4.50	5718
HD 38207	F2 V	0.05	0.00	4.50	6762
HD 38529	G8 III/IV	0.00	0.00	4.50	5361
HD 38949	G1 V	0.00	0.00	4.50	6028
HD 40647	G5	0.00	0.00	4.50	5268
HD 41700	F8/G0 V	0.00	0.00	4.50	6138
HD 43989	G0 V	0.00	0.00	4.47	5958
HD 44594	G3 V	0.00	0.00	4.50	5784

TABLE 5—*Continued*

Source	Spectral Type	A_V (mag)	[Fe/H] (dex)	$\log g$ (log cm s^{-2})	$T_{\rm eff}$ (K)
HD 45270	G1 V	0.00	0.00	4.47	5885
HD 47875	G3 V	0.34	0.00	4.47	5825
HD 60737	G0	0.00	0.00	4.50	5895
HD 61005	G8 Vk	0.00	0.00	4.50	5463
HD 61994	G6 V	0.00	0.00	4.50	5538
HD 64324	G0	0.00	0.00	4.50	5737
HD 66751	F8 V	0.00	0.00	4.50	5854
HD 69076	K0 V	0.00	0.00	4.50	5405
HD 70516	G0	0.00	0.00	4.54	5735
HD 70573	G1/2 V	0.04	0.00	4.47	5896
HD 71974	G5	0.00	0.00	4.50	5436
HD 72687	G5 V	0.00	0.00	4.50	5738
HD 72905	G1.5 VB	0.00	0.00	4.50	5834
HD 73668	G1 V	0.00	0.00	4.50	5876
HD 75302	G5 V	0.00	0.00	4.50	5674
HD 75393	F7 V	0.00	0.00	4.50	6055
HD 76218	G9−V	0.00	0.00	4.50	5359
HD 77407	G0(V)	0.00	0.00	4.53	5734
HD 80606	G5	0.12	0.00	4.50	5668
HD 85301	G5	0.00	0.00	4.50	5611
HD 86356	G6/K0	0.40	0.00	4.54	5485
HD 88201	G0 V	0.00	0.00	4.50	6079
HD 88742	G0 V	0.00	0.00	4.50	5954
HD 90712	G2/3 V	0.00	0.00	4.50	5873
HD 90905	G1 V	0.00	0.00	4.50	6028
HD 91782	G0	0.00	0.00	4.50	6107
HD 91962	G1 V	0.00	0.00	4.50	5623
HD 92788	G6 V	0.00	0.00	4.50	5681
HD 92855	F9 V	0.00	0.00	4.50	5981
HD 95188	G8 V	0.00	0.00	4.50	5400
HD 98553	G2/3 V	0.00	0.00	4.50	5917
HD 100167	F8	0.00	0.00	4.50	5779
HD 101472	F7 V	0.00	0.00	4.50	6184
HD 101959	G0 V	0.00	0.00	4.50	6048
HD 102071	K0 V	0.00	0.00	4.50	5297
HD 103432	G6 V	0.00	0.00	4.50	5597
HD 104467	G5 III/IV	0.13	0.00	4.06	5681
HD 104576	G3 V	0.00	0.00	4.50	5436
HD 104860	F8	0.00	0.00	4.47	5951
HD 105631	G9 V	0.00	0.00	4.50	5343
HD 106156	G8 V	0.00	0.00	4.50	5403
HD 106252	G0 V	0.00	0.00	4.50	5876
HD 106772	G2 III/IV	0.00	0.00	4.50	4928
HD 107146	G2 V	0.00	0.00	4.50	5841
HD 107441	G1.5 IV	0.28	0.00	4.21	5926
HD 108799	G1/2 V	0.00	0.00	4.50	5815
HD 108944	F9 V	0.00	0.00	4.50	6138
HD 111170	G8/K0 V	0.41	0.00	4.35	5384
HD 112196	F8 V	0.00	0.00	4.47	5950
HD 115043	G1 V	0.00	0.00	4.50	5846
HD 116099	G0/3	0.07	0.00	4.21	5899
HD 117524	G2.5 IV	0.62	0.00	4.21	5902
HD 119269	G3/5 V	0.14	0.00	4.21	5732
HD 120812	F8/G0 V	0.37	0.00	4.12	6081
HD 121320	G5 V	0.00	0.00	4.50	5637
HD 121504	G2 V	0.00	0.00	4.50	5967
HD 122652	F8	0.00	0.00	4.50	6163
HD 126670	G6/8 III/IV	0.29	0.00	4.26	5528
HD 128242	G3 V	0.36	0.00	4.26	5823
HD 129333	G5 V	0.00	0.00	4.54	5653
HD 132173	G0 V	0.00	0.00	4.50	5980
HD 133295	G0/1 V	0.00	0.00	4.50	6003
HD 133938	G6/8 III/IV	0.31	0.00	4.26	5566
HD 134319	G5(V)	0.00	0.00	4.54	5660
HD 135363	G5(V)	0.00	0.00	4.66	4728
HD 136923	G9 V	0.00	0.00	4.50	5343

TABLE 5—*Continued*

Source	Spectral Type	A_V (mag)	[Fe/H] (dex)	$\log g$ ($\log$ cm s^{-2})	$T_{\rm eff}$ (K)
HD 138004	G2 III	0.00	0.00	4.50	5715
HD 139498	G8(V)	0.26	0.00	4.26	5473
HD 139813	G5	0.00	0.00	4.50	5380
HD 140374	G8 V	0.09	0.00	4.26	5444
HD 141521	G8 V	0.06	0.00	4.26	5450
HD 141937	G2/3 V	0.00	0.00	4.50	5844
HD 141943	G0/2 V	0.14	0.00	4.23	5943
HD 142229	G5 V	0.00	0.00	4.50	5861
HD 142361	G3 V	0.46	0.00	3.70	5846
HD 143006	G6/8	0.58	0.00	3.70	5817
HD 143358	G1/2 V	0.01	0.00	4.12	5899
HD 145229	G0	0.00	0.00	4.50	5895
HD 146516	G0 IV	0.83	0.00	3.70	6024
HD 150554	F8	0.00	0.00	4.50	5975
HD 150706	G3(V)	0.00	0.00	4.50	5885
HD 151798	G3 V	0.00	0.00	4.47	5878
HD 152555	F8/G0 V	0.00	0.00	4.50	5891
HD 153458	G5 V	0.00	0.00	4.50	5768
HD 154417	F9 V	0.00	0.00	4.50	6014
HD 157664	G0	0.05	0.00	4.50	6251
HD 159222	G1 V	0.00	0.00	4.50	5774
HD 161897	K0	0.00	0.00	4.50	5558
HD 167389	F8(V)	0.00	0.00	4.50	5846
HD 170778	G5	0.00	0.00	4.50	5893
HD 172649	F5	0.00	0.00	4.50	6172
HD 174656	G6 IV	0.83	0.00	3.95	5628
HD 179949	F8 V	0.00	0.00	4.50	6116
HD 183216	G2 V	0.00	0.00	4.50	6002
HD 187897	G5	0.00	0.00	4.50	5883
HD 190228	G5 IV	0.00	0.00	4.50	5246
HD 191089	F5 V	0.00	0.00	4.50	6450
HD 193017	F6 V	0.00	0.00	4.50	6121
HD 195034	G5	0.00	0.00	4.50	5800
HD 199019	G5	0.00	0.00	4.50	5485
HD 199143	F8 V	0.00	0.00	4.23	5895
HD 199598	G0 V	0.00	0.00	4.50	5882
HD 200746	G5	0.00	0.00	4.50	5701
HD 201219	G5	0.00	0.00	4.50	5610
HD 201989	G3/5 V	0.00	0.00	4.50	5636
HD 202108	G3 V	0.00	0.00	4.50	5722
HD 202917	G5 V	0.00	0.00	4.50	5555
HD 203030	G8 V	0.00	0.00	4.50	5416
HD 204277	F8 V	0.00	0.00	4.50	6189
HD 205905	G2 V	0.00	0.00	4.50	5925
HD 206374	G6.5 V	0.00	0.00	4.50	5577
HD 209253	F6/7 V	0.00	0.00	4.50	6211
HD 209393	G5	0.00	0.00	4.50	5632
HD 209779	G2 V	0.00	0.00	4.50	5575
HD 212291	G5	0.00	0.00	4.50	5622
HD 216275	G0	0.00	0.00	4.50	5956
HD 216803	K4 VP	0.00	0.00	4.50	4624
HD 217343	G3 V	0.00	0.00	4.47	5772
HD 219498	G5	0.07	0.00	4.50	5666
HD 224873	K0	0.00	0.00	4.50	5181
HD 245567	G0 V	0.61	0.00	3.91	6042
HD 279788	G5 V	0.63	0.00	3.80	5713
HD 281691	K1(V)	0.16	0.00	4.38	5127
HD 282346	G8 V	0.55	0.00	4.50	5475
HD 284135	G3(V)	0.08	0.00	4.03	5799
HD 284266	K0(V)	0.08	0.00	4.34	5426
HD 285281	K1	0.69	0.00	4.32	5135
HD 285372	K3(V)	0.72	0.00	4.21	5039
HD 285751	K2(V)	0.47	0.00	4.21	5017
HD 285840	K1(V)	0.00	0.00	4.61	5165
HD 286179	G3(V)	0.38	0.00	4.21	5843
HD 286264	K2 IV	1.11	0.00	4.49	4991

TABLE 5—*Continued*

Source	Spectral Type	A_V (mag)	[Fe/H] (dex)	$\log g$ (log cm s^{-2})	$T_{\rm eff}$ (K)
HE 350	...	0.31	0.00	4.47	5922
HE 373	...	0.31	0.00	4.60	5399
HE 389	...	0.31	0.00	4.47	6043
HE 622	...	0.31	0.00	4.54	5497
HE 696	...	0.31	0.00	4.54	5756
HE 699	...	0.31	0.00	4.54	5634
HE 750	F5	0.31	0.00	4.33	6421
HE 767	...	0.31	0.00	4.40	6219
HE 848	F9 V	0.31	0.00	4.40	6309
HE 935	F9.5 V	0.31	0.00	4.40	6115
HE 1101	...	0.31	0.00	4.47	5823
HE 1234	G2	0.31	0.00	4.54	5738
HII 120	G6 V	0.12	0.00	4.50	5707
HII 152	G5 V	0.12	0.00	4.50	5823
HII 173	...	0.12	0.00	4.50	5266
HII 174	...	0.12	0.00	4.50	4998
HII 250	...	0.12	0.00	4.50	5767
HII 314	...	0.12	0.00	4.50	5788
HII 514	...	0.12	0.00	4.50	5727
HII 1015	...	0.12	0.00	4.50	5904
HII 1101	G0 V	0.12	0.00	4.50	5988
HII 1182	F8	0.12	0.00	4.50	5845
HII 1200	F6 V	0.12	0.00	4.50	6217
HII 1776	G5	0.12	0.00	4.50	5622
HII 2147	G7 IV	0.12	0.00	4.50	5089
HII 2278	...	0.12	0.00	4.50	5213
HII 2506	F9	0.12	0.00	4.50	6082
HII 2644	...	0.12	0.00	4.50	5614
HII 2786	...	0.12	0.00	4.50	6068
HII 2881	K2	0.12	0.00	4.50	4844
HII 3097	...	0.12	0.00	4.50	5585
HII 3179	...	0.12	0.00	4.50	6137
HIP 6276	G0	0.00	0.00	4.50	5352
HIP 42491	G5	0.00	0.00	4.50	5246
HIP 59154	K2	0.00	0.00	4.50	4390
HIP 76477	G9	0.43	0.00	4.38	5389
MML 1	K1+IV	0.56	0.00	4.44	5150
MML 8	K0+IV	0.48	0.00	4.35	5278
MML 9	G9 IV	0.34	0.00	4.35	5360
MML 17	G0 IV	0.28	0.00	4.21	6002
MML 18	K0+IV	0.61	0.00	4.35	5290
MML 26	G5 IV	0.33	0.00	4.21	5711
MML 28	K2−IV	0.06	0.00	4.44	4970
MML 32	G1 IV	0.61	0.00	4.21	5991
MML 36	K0 IV	0.27	0.00	4.38	5271
MML 38	G8 IVe	0.45	0.00	4.26	5487
MML 40	G9 IV	0.45	0.00	4.38	5382
MML 43	G7 IV	0.36	0.00	4.26	5525
MML 51	K1 IVe	0.67	0.00	4.38	5142
MML 57	G1.5 IV	0.21	0.00	4.12	5913
PDS 66	K1 IVe	0.57	0.00	4.35	5256
[PZ99] J155847.8−175800	K3	1.41	0.00	4.22	4889
[PZ99] J160814.7−190833	K2	1.06	0.00	4.19	4997
[PZ99] J161318.6−221248	G9	1.22	0.00	4.06	5396
[PZ99] J161329.3−231106	K1	1.25	0.00	4.19	5154
[PZ99] J161402.1−230101	G4	1.35	0.00	4.06	5783
[PZ99] J161411.0−230536	K0	1.15	0.00	4.16	5312
[PZ99] J161459.2−275023	G5	0.95	0.00	4.06	5724
[PZ99] J161618.0−233947	G7	0.83	0.00	4.06	5553
QT And	K7 Ve	0.00	0.00	4.62	4692
R3	...	0.12	0.00	4.61	5214
R45	...	0.12	0.00	4.47	5947
R83	...	0.12	0.00	4.47	5796
RE J0137+18A	K3 Ve	1.47	0.00	4.38	5001
RE J0723+20	K5 VE	0.00	0.00	4.50	4408
RX J0258.4+2947	K0 IV	0.41	0.00	4.61	5274

TABLE 5—*Continued*

Source	Spectral Type	A_V (mag)	[Fe/H] (dex)	$\log g$ (log cm s^{-2})	$T_{\rm eff}$ (K)
RX J0329.1+0118	G0(IV)	0.04	0.00	4.50	6150
RX J0331.1+0713	K4(V)/E	0.08	0.00	4.01	4777
RX J0354.4+0535	G2(V)	0.01	0.00	4.47	5846
RX J0357.3+1258	G0	0.59	0.00	4.47	6037
RX J0434.3+0226	K4e	0.37	0.00	4.63	4666
RX J0442.5+0906	G5(V)	0.45	0.00	4.54	5700
RX J0849.2−7735	K2	0.00	0.00	4.50	4382
RX J0850.1−7554	G5	0.31	0.00	4.54	5713
RX J0853.1−8244	K0(V)	0.65	0.00	4.50	5317
RX J0917.2−7744	G2	0.32	0.00	4.47	5888
RX J1111.7−7620	K1	1.50	0.00	4.21	4653
RX J1140.3−8321	K2	0.67	0.00	4.67	4970
RX J1203.7−8129	K1	0.46	0.00	4.50	5229
RX J1209.8−7344	G9	1.46	0.00	4.50	5426
RX J1220.6−7539	K2	0.54	0.00	4.67	4997
RX J1225.3−7857	G5	0.50	0.00	4.50	5732
RX J1450.4−3507	K1(IV)	0.52	0.00	4.38	5158
RX J1457.3−3613	G6 IV	0.32	0.00	4.26	5590
RX J1458.6−3541	K3(IV)	0.56	0.00	4.44	4852
RX J1500.8−4331	K1(IV)	0.28	0.00	4.38	5158
RX J1507.2−3505	K0	0.24	0.00	4.38	5263
RX J1518.4−3738	K1	0.37	0.00	4.38	5166
RX J1531.3−3329	K0	0.13	0.00	4.50	5304
RX J1541.1−2656	G7	0.66	0.00	4.06	5542
RX J1544.0−3311	K1	0.36	0.00	4.38	5150
RX J1545.9−4222	K1	0.56	0.00	4.38	5143
RX J1600.6−2159	G9	0.80	0.00	4.06	5375
RX J1839.0−3726	K1	0.41	0.00	4.45	5119
RX J1841.8−3525	G7	0.16	0.00	4.34	5534
RX J1842.9−3532	K2	1.06	0.00	4.27	4645
RX J1844.3−3541	K5	0.15	0.00	3.91	4648
RX J1852.3−3700	K3	0.97	0.00	4.31	4854
RX J1917.4−3756	K2	0.44	0.00	4.21	5033
RX J2313.0+2345	F8	0.16	0.00	4.01	6105
SAO 150676	G2 V	0.02	0.00	4.47	5862
SAO 178272	K2 V	0.42	0.00	4.50	4963
ScoPMS 21	K1 IV	1.58	0.00	3.70	5806
ScoPMS 27	K2 IV	1.10	0.00	4.19	5066
ScoPMS 52	K0 IV	1.54	0.00	4.06	5372
ScoPMS 214	K0 IV	1.75	0.00	4.16	5331
V343 Nor	K0 V	0.00	0.00	4.38	5002
V383 Lac	K0 IV	0.00	0.00	4.67	5121
W79	...	0.12	0.00	4.61	5415
vB 1	F8	0.00	0.13	4.50	5983
vB 39	G4 V	0.00	0.13	4.50	5633
vB 49	G0 V	0.00	0.13	4.50	5927
vB 52	G2 V	0.00	0.13	4.50	5841
vB 63	G1 V	0.00	0.13	4.50	5694
vB 64	G2+	0.00	0.13	4.50	5733
vB 66	F8	0.00	0.13	4.50	6058
vB 73	G2 V	0.00	0.13	4.50	5926
vB 79	K0 V	0.00	0.13	4.50	5273
vB 88	F9 V	0.00	0.13	4.50	6107
vB 91	...	0.00	0.13	4.50	5021
vB 92	...	0.00	0.13	4.50	5514
vB 93	K2 V	0.00	0.13	4.50	5112
vB 96	G5	0.00	0.13	4.50	5165
vB 97	F8:V:	0.00	0.13	4.50	5873
vB 99	K0	0.00	0.13	4.50	5156
vB 106	G5	0.00	0.13	4.50	5782
vB 142	G5	0.00	0.13	4.50	5652
vB 143	F8	0.00	0.13	4.50	6228
vB 176	K2 V	0.00	0.13	4.50	4942
vB 180	K1 V	0.00	0.13	4.50	5216
vB 183	K2 V	0.00	0.13	4.50	5037

C1. OPTICAL AND NEAR-INFRARED PHOTOMETRY

Synthetic spectra were normalized to published optical and near-infrared broadband photometry. Photometric catalogs incorporated for this study include Tycho-2 (Høg et al. 2000), *Hipparcos* (Perryman et al. 1997), 2MASS (Skrutskie et al. 2006), and the General Catalogue of Photometric Data (GCPD; Mermilliod et al. 1997). The GCPD is a compilation of published ground based observations that includes, among many others, *UBV* Johnson, *RI* Cousins and Kron, and Stromgren *uvby*. The GCPD data are of nonuniform quality compared to these other surveys.

Ground-based infrared photometry from the *ISO* preparatory observations in both the ESO and Tenerife photometric systems[19] were also included. Finally, the FEPS team obtained *BRVI* photometry for several stars that did not have high-quality photometry available in the literature. The observations, data reduction, and measured photometry for these sources are presented in Appendix A.

C2. SYNTHETIC PHOTOMETRY

For wavelengths longer than 10 μm, the original Kurucz synthetic spectra are sampled at 10.02 μm, and then between 20 and 160 μm in steps of 20 μm. For wavelengths longer than 10 μm, we resampled the Kurucz spectra at finer wavelengths by interpolating between model data points assuming a $S_\nu \propto \nu^2$ spectrum.

Synthetic fluxes were computed by multiplying a Kurucz synthetic spectrum with the spectral response of a photometric system. The spectral response, $T(\lambda)$, includes the detector quantum efficiency, the atmospheric transmission (if appropriate), the filter transmission, and any other optics whose characterizations are available (see Cohen et al. 1999 for details). The product of these three transmission functions are referred to as a FAD (i.e., filter+atmosphere+detector).

By definition, the bandwidth of the filter in wavelength and frequency units is

$$\Delta\lambda = \int T(\lambda)/T_{\max}\, d\lambda, \tag{C1}$$

$$\Delta\nu = \int T(\lambda)/T_{\max}\, d\nu, \tag{C2}$$

where $T_{\max}$ is the peak transmission. Uncertainties in the bandwidths were computed by assuming a 5% uncertainty in the transmission at any given wavelength. The spectral irradiance, I, can be computed by integrating the spectrum, $S(\lambda)$, over the FAD as

$$I = \int S(\lambda)T(\lambda)\, d\lambda. \tag{C3}$$

The corresponding (isophotal) flux density is then defined as

$$S_\lambda = I/\Delta\lambda, \tag{C4}$$

$$S_\nu = I/\Delta\nu. \tag{C5}$$

Since observed optical and near-infrared flux densities are typically quoted in magnitudes, the synthetic measurements were converted to magnitudes based on the flux for a zero-magnitude star as

$$m = -2.5\log\left(\frac{S_\lambda}{\mathrm{ZP}}\right) + \mathrm{zpo}, \tag{C6}$$

where ZP is the zero point of the photometric system, and zpo is the offset needed to convert the synthetic photometry to the observed photometric system. Martin Cohen and collaborators have produced a series of papers in which they define the zero points and zero point offsets for several photometric systems. We adopt the calibration by Cohen et al. (2003a) for 2MASS, Cohen et al. (2003b) for Tycho-2, *Hipparcos*, and Landolt *BVRI*, and Cohen et al. (1999) for ESO *HK* and Tenerife *HK*. For Stromgren photometry, we adopt the calibration of Gray (1998) but replace his flux density for Vega at 5556 Å with that of Cohen et al. (1992) for consistency.

C3. FITTING PROCEDURE

The χ^2 merit equation to determine the best fit Kurucz model is

$$\chi^2 = \sum_{i=1}^{N}\left\{\frac{\left[F_{i,\mathrm{obs}} - F_{i,\mathrm{model}}(T_{\mathrm{eff}}, \mathrm{A_V}, [\mathrm{Fe/H}],\ \log g, \Omega)\right]^2}{\left(\Delta F_{i,\mathrm{obs}}^2 + \Delta F_{i,\mathrm{model}}^2\right)}\right\} + \left(\frac{T_{\mathrm{eff}} - T_{\mathrm{eff,o}}}{\Delta T_{\mathrm{eff,o}}}\right)^2, \tag{C7}$$

where $F_{i,\mathrm{obs}}$ is the observed flux density typically expressed in magnitudes, $F_{i,\mathrm{model}}$ is the model flux density that depends on the stellar effective temperature (T_{eff}), visual extinction (A_V), metallicity ([Fe/H]), surface gravity ($\log g$), and solid angle (Ω), and $T_{\mathrm{eff,o}}$ is the nominal temperature of the star derived from the spectral type (if available).

[19] See http://www.iso.vilspa.esa.es/users/expl_lib/ISO/wwwcal/isoprep/gbpp/photom.

Equation (C7) was minimized using a modified version of the Levenberg-Marquardt method as implemented by the LMDIF routine in the MINPACK library.[20] The model parameters are the solid angle of the star, the effective temperature, surface gravity, metallicity, and visual extinction. In practice, the metallicity and surface gravity was fixed to the values listed in Table 5. The constraint in the fitting procedure is that the visual extinction is nonnegative. The initial values for A_V and $T_{\rm eff}$ were set based on the stellar properties (see Appendix B).

Fits were constrained using photometry at wavelengths between 0.4 and 2.5 μm for most sources. A few sources have excesses at *K*-band (Silverstone et al. 2006) and the model was fitted to photometry between 0.4 and 1.2 μm. Shorter wavelength photometry, in particular *U*-band observations, were omitted since those data are difficult to calibrate from the ground and are sensitive to the stellar metallicity. Longer wavelengths were omitted to avoid having infrared excesses bias the model fits.

Uncertainties in the model flux densities were computed using a grid search around the best-fit model parameters. The size of the grid was ± 3 times the nominal parameter uncertainties computed from the covariance matrix computed from the least-squares fit. At each point in the model grid, we computed model flux densities, including the *Spitzer* IRAC and MIPS photometric bands, as well as the χ^2 between that model and the observed flux densities for photometric bands between 0.4 and 2.5 μm. The relative probability that the model at a given grid point can reproduce the observations is $e^{-\chi^2/2}$. The probabilities over all grid points then yields the probability distribution of model flux densities.

It is not feasible to present the full probability distribution for each *Spitzer* photometric band and each star. We instead characterized the probability distribution for a photometric band by the nominal flux density, $F_{\rm model}$, and the 1 σ uncertainty $\Delta F_{\rm model}$. The nominal flux density is given by the flux density computed from the best-fit model parameters. The 1 σ flux uncertainty is defined as the smallest range of model flux densities about $F_{\rm model}$ that encompasses 68% of the total probability. Results from the Kurucz-model fitting have been used by Kim et al. (2005), Hines et al. (2006), and Hillenbrand et al. (2008).

[20] See http://www.netlib.org/minpack.

REFERENCES

Ardila, D. R., et al. 2004, ApJ, 617, L147
Bouwman, J., et al. 2008, ApJ, 683, 479
Breger, M. 1986, ApJ, 309, 311
Carpenter, J. M., Wolf, S., Schreyer, K., Launhardt, R., & Henning, T. 2005, AJ, 129, 1049
Carpenter, J. M., et al. 2008, ApJ, submitted (arXiv: 0810.1003)
Chen, B., Vergely, J. L., Valette, B., & Carraro, G. 1998, A&A, 336, 137
Cohen, M., Megeath, S. T., Hammersley, P. L., Martín-Luis, F., & Stauffer, J. 2003a, AJ, 125, 2645
Cohen, M. Walker, R. G., Barlow, M. J., & Deacon, J. R. 1992, AJ, 104, 1650
Cohen, M., Walker, R. G., Carter, B., Hammersley, P. L., Kidger, M., & Noguchi, K. 1999, AJ, 117, 1864
Cohen, M., Wheaton, W. A., & Megeath, S. T. 2003b, AJ, 126, 1090
Crawford, D., & Barnes, J. 1974, AJ, 79, 687
D'Antona, F., & Mazzitelli, I. 1997, Mem. Soc. Astron. Italiana, 68, 807
Engelbracht et al. 2007, PASP, 119, 994
Evans, N. J., II, et al. 2003, PASP, 115, 965
Fazio, G., Hora, J. L, Allen, L. E., et al. 2004, ApJS, 154, 10
Gordon, K. D., et al. 2007, PASP, 119, 1019
Gray, D. F. 1992, The Observation and Analysis of Stellar Photospheres (Cambridge: Cambridge Univ. Press)
Gray, R. O. 1998, AJ, 116, 482
Hampel, F. 1974, J. AM. Statist. Assoc., 69, 383
Hillenbrand, L. A., et al. 2008, ApJ, 677, 630
Hines, D. C., et al. 2006, ApJ, 638, 1070
Hollenbach, D., et al. 2005, ApJ, 631, 1180
Høg, E., et al. 2000, A&A, 355, L27
Houck, J., et al. 2004, ApJS, 154, 18
Houdashelt, M. L., Bell, R. A., & Sweigart, A. V. 2000, AJ, 119, 1448
Kenyon, S. H.,\& Hartmann, L. 1995, ApJS, 101, 117
Kim, J. S., et al. 2005, ApJ, 632, 659
Landolt, A. U. 1992, AJ, 104, 340
Makovoz, D., & Marleau, F. R. 2005, PASP, 117, 1113
Mamajek, E. E., Meyer, M. R., & Liebert, J. 2002, AJ, 124, 1670
———. 2006, AJ, 131, 2360
Mathis, J. S. 1990, ARA&A, 28, 37
Mermilliod, J.-C., Mermilliod, M., & Hauck, B. 1997, A&AS, 124, 349
Meyer, M. R., et al. 2004, ApJS, 154, 422
———. 2006, PASP, 118, 1690
Meyer, M. R., et al. 2008, ApJ, 673, L181
Moro-Martín, A., et al. 2007, ApJ, 658, 1312
Nagao, M., & Matsuyama, T. 1979, Comput. Graphics Image Processing, 9, 394
Naylor, T. 1998, MNRAS, 296, 339
Pascucci, I., et al. 2006, ApJ, 651, 1177
———. 2007, ApJ, 663, 383
Paulson, D. B., Sneden, C., & Cochran, W. D. 2003, AJ, 125, 3185
Perryman, M. A. C., et al. 1997, A&A, 323, L49
Pinsonneault, M. H., Stauffer, J., Soderblom, D. R., King, J. R., & Hanson, R. B. 1998, ApJ, 504, 170
Prosser, C. F. 1992, AJ, 103, 488
Reach, W. T., et al. 2005, PASP, 117, 978
Rieke, G., et al. 2004, ApJS, 154, 25
———. 2008, AJ, 135, 2245
Sandage, A. 1972, ApJ, 178, 1
Silverstone, M. D., et al. 2006, ApJ, 639, 1138
Skrutskie, M. F., et al. 2006, AJ, 131, 1163
Stauffer, J. R., et al. 2005, AJ, 130, 1834
Taylor, B. J. 1986, ApJS, 60, 577
———. 2006, AJ, 132, 2453
Welsh, B. Y., Crifo, F., & Lallement, R. 1998, A&A, 333, 101
Werner, M., et al. 2004, ApJS, 154, 1
Whiteoak, J. B. 1961, MNRAS, 123, 245
Williams, J. P., Najita, J., Liu, M. C., Bottinelli, S., Carpenter, J. M., Hillenbrand, L. A., Meyer, M. R., & Soderblom, D. R. 2004, ApJ, 604, 414
Wright, C. O., Egan, M. P., Kraemer, K. E., & Price, S. D. 2003, AJ, 125, 349
Zacharias, N., Urban, S. E., Zacharias, M. I., Wycoff, G. L., Hall, D. M., Monet, D. G., & Rafferty, T. J. 2004, AJ, 127, 3043